Numerical and experimental investigations on the welding residual stresses and distortions of the short fillet welds in high strength steel plates

Ghafouri Mehran, Ahola Antti, Ahn Joseph, Björk Timo

DOI: 10.1016/j.engstruct.2022.114269

Engineering Structures 260 (2022) 114269

Contents lists available at ScienceDirect

Engineering Structures

journal homepage: www.elsevier.com/locate/engstruct

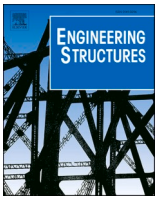

Numerical and experimental investigations on the welding residual stresses and distortions of the short fillet welds in high strength steel plates

Mehran Ghafouri [a,*], Antti Ahola [a], Joseph Ahn [b], Timo Björk [a]

[a] Laboratory of Steel Structures, School of Energy Systems, LUT University, P.O. Box 20, 53851 Lappeenranta, Finland
[b] Department of Mechanical Engineering, Imperial College London, South Kensington Campus, London SW7 2AZ, UK

ARTICLE INFO

Keywords:
Welding simulation
Welding residual stress
High strength steel
Welding distortion
Finite element simulation

ABSTRACT

The current study investigates the influence of different welding sequences and external constraints on development of welding- induced angular distortion and residual stresses in the short fillet welds made of the high strength steel (HSS), S700, using the finite element (FE) method. Three-dimensional thermo-elastic-plastic FE modeling was performed in the ABAQUS FE software based on the double-ellipsoidal heat source model, temperature-dependent material properties, and considering geometrical non-linearity. The accuracy of the FE models were verified by comparing the simulation results and experimentally measured data. Both the numerical method and measurements show that external constraint has relatively larger influence than welding sequence on the development of angular distortion and the peak magnitude of residual stresses. To determine the significance of short fillet welds in terms of induced distortion and residual stress fields, the results captured by simulation and validated by measurements were compared to those of continuous fillet welds. From a numerical point of view, the results of this study are meaningful to understand the reasonable accuracy required to capture the necessary details of the welding process. From an engineering prospect, the results of this study can be important as they indicate that transverse residual stress fields due to short fillet welds are localized with considerably larger peak magnitudes compared to continuous fillet welds. With respect to the angular distortion, the results of this study show that stiffness of external constraint has a greater impact on prevention of angular distortion in continuous fillet welds than in short fillet welds. In the case of fillet welds with small lengths, beside proper clamping, other deformation control techniques such as pre-alignment of the welded members need to be considered.

1. Introduction

In the world of construction and manufacturing, steel is one of the main construction materials. Steel production is claimed to be the largest energy consumer among the industrial sectors. The process is highly energy intensive with consequential environmental impacts [1]. It is of paramount importance to make balance between the environmental impacts from one side and huge demands for such materials from the other side. In this respect, one environmental energy solution is to increase the strength level of steels, which has contributed to the advent of lightweight and high-performance materials. This insight has triggered the development of high and ultra-high strength steels (HSS/UHSS). Remarkable features of these materials such as high strength to weight ratio, desirable weldability and toughness, makes them highly applicable in a wide variety of industrial applications, such as the oil and gas industries, offshore construction, automotive and shipbuilding industries [2].

Due to its advantages over mechanical joining methods, the fusion welding process has been widely used in the construction and manufacturing industries to fabricate large structures and assemblies. Weight reduction, enhanced structural performance and flexibility in design, and cost-effectiveness can be named among the advantages attributed to the fusion welding technology [3]. Arc welding processes and among them gas metal arc welding (GMAW), which is categorized as a fusion welding technique, has been extensively utilized to permanently join structural members and components made from HSSs [2]. Fusion welding, however, is a complex thermal process, which transports highly concentrated and tremendous heat input to the welded joint. This uneven temperature field followed by a non-linear cooling in the weld zone, can cause serious strength problems such as heat-affected

* Corresponding author.
E-mail address: mehran.ghafouri@lut.fi (M. Ghafouri).

https://doi.org/10.1016/j.engstruct.2022.114269
Received 7 December 2021; Received in revised form 15 March 2022; Accepted 10 April 2022
Available online 19 April 2022

Table 1
The chemical compositions of S700MC PLUS and ESAB OK AristoRod 13.29 (wt. %).

Material	C	Si	Mn	P	S	Al	Ti	Cr	Ni	Mo	Nb	V
S700 MC	0.12	0.25	2.10	0.02	0.01	0.015	0.15				0.09	0.2
AristoRod 13.29	0.089	0.53	1.54	–	–	–	–	0.26	1.23	0.24	–	–

zone (HAZ) softening [4] and rise of residual stresses and distortions [5]. Welding residual stresses can be detrimental or beneficial depending on magnitude, distribution or sign of stresses [6]. Tensile residual stresses are harmful and directly affect fatigue performance and service life of welded connections [7–9]. Stress corrosion cracking [10], which contributes to degradation of the structural integrity of welded joints, and decreased buckling strength [11] are attributed to the presence of tensile residual stresses. Welding deformation is a technical challenge resulting in dimensional inaccuracy and leads to decrease the quality of the welded joint. By imposing correction work, welding deformation can cause fabrication delays, incur financial cost, and decrease productivity. Excessive deformation might seriously impair fabrication, and, in extreme cases, lead to failure [12].

Reliable design of steel structures and ensuring safety to their applications necessitates evaluation of welding residual stresses and distortions. Measurement of residual stress in the literature has been reported by means of different destructive and non-destructive techniques such as hole-drilling [13,14], crack compliance [15], XRD [6,16], and Neutron diffraction techniques [17–20]. Assessment of residual stresses by means of experimental methods post welding is available, However, those methods in general have their own challenges. Destructive methods, such as the hole drilling technique, are inapplicable and non-destructive methods have their own limitations in terms of accessibility, such as the X-ray diffraction (XRD) method.

The privilege of the numerical methods over the experimental methods is the ability of computational techniques in prediction of residual stress state and welding deformation patterns before the real welds are applied. Although development of welding residual stresses and distortions can hardly be avoided, accurate prediction makes it possible to adopt engineering measures to reduce welding deformations and stresses. This matter, especially in terms of HSSs where rapid heating and cooling inherent to welding can seriously degenerate their high load bearing capacity, is of particular importance.

During the past decades, a number of studies have been done concerning elaboration of the computational methods to predict welding residual stresses and deformations. As a numerical approach, the FE method has proven its ability to solve a broad spectrum of engineering and scientific problems and is frequently used in the field of welding simulation. FE simulation of different welding processes [6,16,17,21–23] for a wide range of materials [13,15,24–28] have been accomplished.

Fillet weld is known to be one of the most prevalent weld types used in the fabrication of a broad range of steel structures such as plate girders and stiffened panels. Fillet welded joints either single or double sided, may suffer from different welding deformation types, such as transverse and longitudinal shrinkages, and angular distortion [29]. Depending on the design and applied load, in order to reduce the labor cost and weight of the stiffened panels, an alternative method of attaching the stiffener to the base plate is non-continuous welding, which is also known as intermittent welding [30]. During the fabrication of steel structures in the assembly stage, making temporary connections between the structural members is performed through tack welds, which can also be considered as short welds. From the tack welding viewpoints, it is also important to understand the formation of welding distortions under different tack welding sequences and boundary conditions, as they might be considered in manufacturing, for example, by pre-alignments or changing the welding sequence. Although there has been several research on welding simulation of T-fillet welded steel joints [29,31–34], till present there is lack of data regarding the welding distortions and residual stresses developed due to short fillet welds in HSSs under the influence of different external restraints and welding sequences.

Table 2
The nominal mechanical properties of S700MC PLUS and ESAB OK AristoRod 13.29.

Material	Yield strength σ_y[MPa]	Ultimate tensile strength σ_u[MPa]	Elongation %
S700 MC PLUS	700	750–950	13
AristoRod 13.29	700	800	19

The aim of this research is prediction and evaluation of welding stresses and angular distortion developed in the T-joints made of HSS S700MC PLUS due to short fillet welds under different external constraints and welding sequences. The matter is accomplished by developing three-dimensional sequentially coupled thermal-structural FE models in ABAQUS code [35]. The temperature field is simulated by considering a moving heat source based on the model proposed by Goldak et al. [36] being implemented in the user-subroutine DFLUX. The combined effects of convection and radiation are considered in modelling the heat loss. Subsequent to capturing the temperature distribution in thermal analysis, the predicted nodal temperatures are transferred into a mechanical model to calculate the welding stresses and angular distortion. The distributions of residual stresses, sequential and final angular distortions due to the external constraints and welding sequences are verified with the experimental measurements, and comparisons are made between the results of the short and continuous fillet welds in terms of thermal and mechanical fields.

2. Experimental setup

2.1. Materials

HSS S700MC PLUS, which is a high strength low carbon and low alloy steel with a minimum yield strength of 700 MPa was used in this study. This material is manufactured by modern hot strip rolling and direct quenching, which differs from the conventional quenching procedures [37]. The filler material for joining the stiffeners to the base plates in this study was ESAB OK AristoRod 13.29 solid wire with 1 mm diameter. This filler material falls in the matching strength level with the base material. Table 1 presents the chemical compositions of the base and filler materials based on the material certificates of the manufacturers. The nominal mechanical properties of the base and filler materials are shown in Table 2.

2.2. Specimens and welding procedure

To investigate the effect of welding sequence and mechanical boundary conditions on deformation characteristics and residual stresses in T-joints connected by short fillet welds, four identical T-joint specimens were fabricated. The dimensions of the base plates and stiffeners being cut from 6 mm hot rolled strips of S700, were 460 × 130 mm and 130 × 25 mm, respectively. Laser cutting of the material was accomplished in such a way that the welding direction was perpendicular to the rolling direction of the base plate. The convention for the welding direction was assumed along the +Y-axis, while Z-axis was normal to the top surface of the base plate. A GMAW robotized arm was

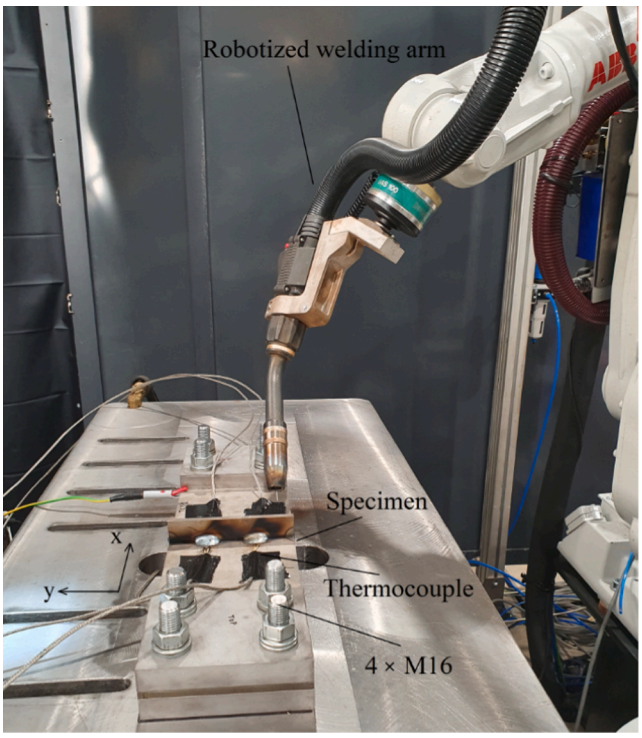

Fig. 1. The experimental set-up of the T-joint specimen.

Table 3
Welding process parameters.

Voltage (V)	Current (A)	Travel speed (mm/s)	Wire diameter (mm)	Wire feed rate (m/min)	Tip distance (mm)	Shielding gas
25	260	7	1	12.5	16	Ar + 8% CO_2

used for welding, as shown in Fig. 1. The torch angle was considered 45° for all the welding cases. Selecting the welding parameters presented in Table 3, the welding leg size of 6 mm was achieved. The net heat input value transported to the joint, amounts to 0.79 kJ/mm by applying a welding efficiency coefficient of 0.85 for GMAW process [38].

The fillet welding procedure included deposition of four weld layers with an approximate length of 20 mm each, on both sides of the specimens. Two different welding sequences were considered to investigate the effect of the welding sequence on the residual stress and deformation patterns, as shown schematically in Fig. 2. The effect of external constraints on welding stresses and deformations were investigated by applying two different clamping set-ups. One configuration was performed so that the specimens were rigidly clamped at both ends (see Fig. 1), while the other clamping restrained the specimens only at one end. Considering the two different welding sequences and external restraints, in total four experimental welding cases were fabricated.

In order to facilitate the discussion and drawing comparisons between the welding cases, to each welding case a label was assigned. In the labelling of specimens, the first letter shows the applied mechanical boundary conditions. That is, **F** indicates the welding cases being clamped at one end, while **C** is used for the cases clamped at both ends. **S1** and **S2** are used to show the welding sequences 1 and 2, respectively. The labels assigned to the welding cases are summarized in Table 4.

2.3. Temperature measurements

Thermal cycles during welding were measured by attaching several K-type thermocouples at different locations on the top surface of each specimen. The positions of thermocouples were arranged so that the high temperature HAZ, and the lower temperature fields far from the

Table 4
Labels assigned to the specimens in welding experiments.

Label	Condition
FS1	One **F**ree end, **S**equence **1**
FS2	One **F**ree end, **S**equence **2**
CS1	Both ends **C**lamped, **S**equence **1**
CS2	Both ends **C**lamped, **S**equence **2**

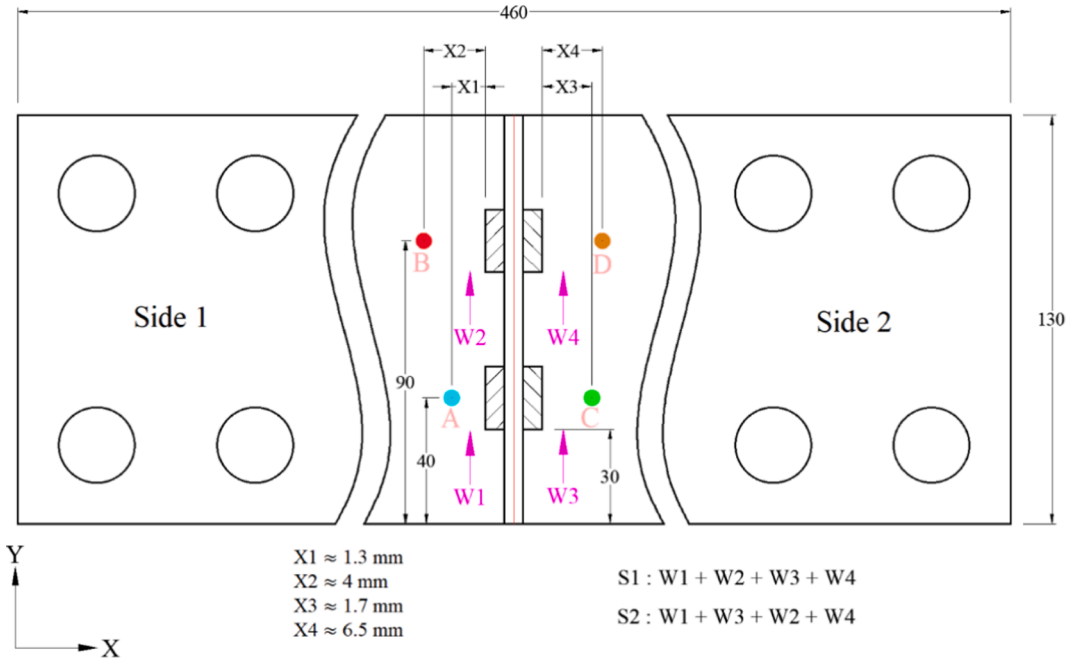

Fig. 2. Illustration of the welding sequences S1 and S2, and the positions of thermocouples. (Units in mm).

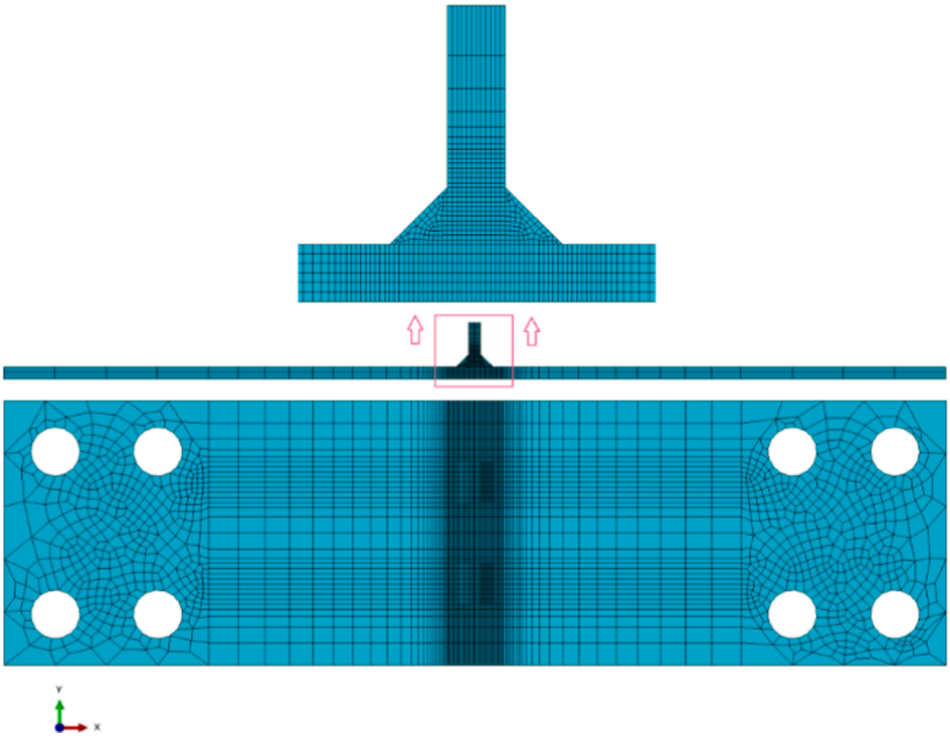

Fig. 3. Mesh details of the fillet welded T-joint.

weld zone can be captured in order to verify the temperature histories obtained from the corresponding FE models. The locations of thermocouples are shown schematically in Fig. 2. As can be seen, four weldments, namely W1–W4, two on each side were produced. The distances of thermocouples A, B, C, and D from the weld toes are shown with X1, X2, X3, and X4, respectively. The accurate values of X1–X4 were determined post welding based on the measurements by a Hexagon 3D scanner in order to make comparisons with the corresponding nodal temperatures from the FE simulations.

3. Finite element simulation

Temperature distribution and evolution of welding deformations and stresses of T-joints due to short fillet welds were investigated by means of the FE method. In this context, three-dimensional thermo-elastic-plastic FE models were developed in ABAQUS FE code. Since the mechanical work performed compared to the thermal energy of the welding arc is negligible, and the structural response under the thermal load has insignificant influence on the temperature field, a sequentially coupled formulation was adopted [39]. In this solution procedure, the heat conduction equation is solved independently from the stress and strain problems. The effect of a non-linear transient temperature field on the mechanical response is considered through the thermal expansion and temperature-dependent mechanical properties of the material. This formulation consists of two steps. In the first step, temperature distribution due to a moving heat source is captured by performing a thermal analysis and solving heat conduction equation. In the next step, the captured nodal temperatures are transferred into a mechanical model and applied as a thermal load to find the mechanical response and compute the developed residual stresses and strains.

3.1. FE model geometry and mesh

All the experimental welding specimens and the amounts of the deposited filler material were identical, however, with different welding sequences and external constraints. In this regard, a 3D FE model with the same mesh structure (see Fig. 3) was developed for all the cases. Nevertheless, the order of element activation varied, which corresponds to the applied welding sequence, and the mechanical boundary conditions applied in accordance with the external restraints. In the thermal analysis, a 1st order 3D 8-node linear diffusive heat transfer brick hexahedron element (DC3D8) with temperature as the only degree of freedom was employed. In order to facilitate the data mapping between the thermal and mechanical models, the same FE mesh with identical number of elements, however different element types were used. In the structural analysis, a 1st order 3D 8-node linear hexahedron reduced integration elements (C3D8R) was used. Shear locking is avoided, better convergence is achieved, and less computational time is required when the reduced integration elements are used [22]. The convergence study on mesh density was carried out in a previous investigation [16] to ensure that the employed mesh structure is sufficiently refined to yield accurate simulation results. Mesh convergence was completed when further refinement of the mesh structure had inconsequential effect on the results. A fine mesh grid with a total number of 28,988 elements was found to be sufficiently accurate to represent the stress and strain results. The smallest element size was 0.5 × 2.5 × 1 mm (in the X, Y, and Z directions), which was applied in the FZ and HAZ, where high tensile residual stresses are expected to be built up. The size of elements increased progressively as the distance from the weld toe towards the outer edges of the specimen increased. Gradual addition of the filler material was simulated using the element birth and death technique, also known as model change in ABAQUS [40]. In this method, the weld metal is divided into several segments. All the elements representing the filler metal are initially inactivated. Based on the assigned step time, when the heat approaches and the relevant segment is heated up, its status is changed from inactive to active to which temperature-dependent thermo-physical properties in the thermal analysis and temperature-deponent mechanical properties in the structural analysis are allocated.

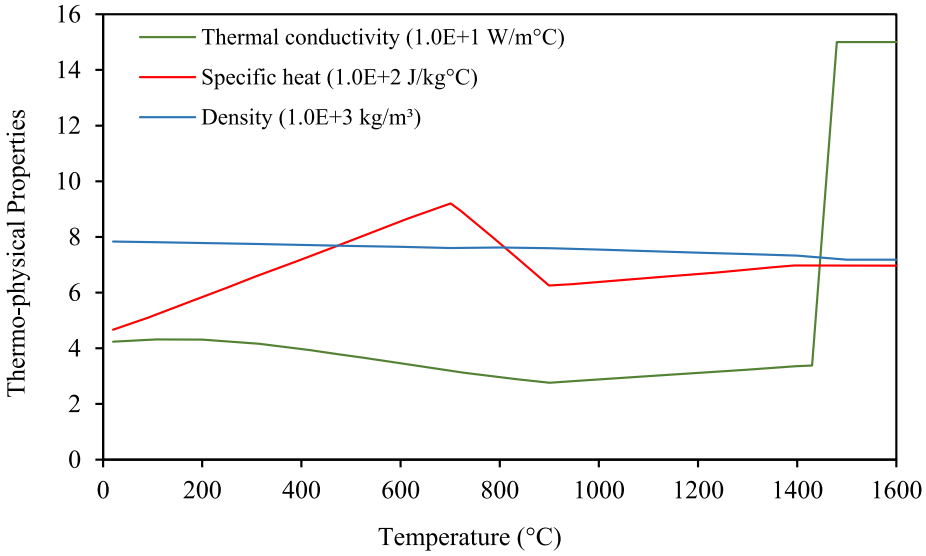

Fig. 4. Temperature-dependent thermo-physical properties of S700.

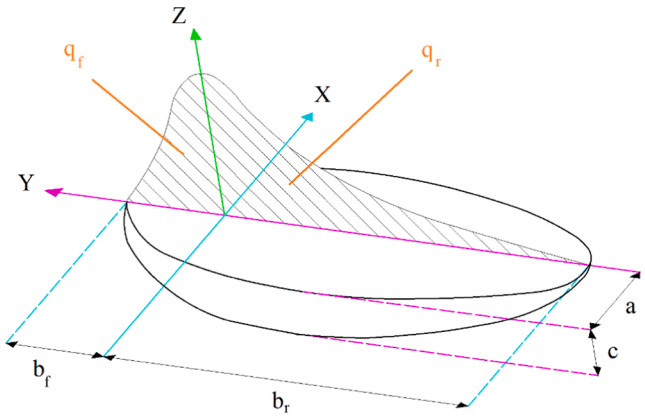

Fig. 5. Schematic of Goldak's volumetric heat source shape.

3.2. Thermal analysis

Transient temperature field during welding (T) in time (t) and space (x, y, z) was solved using a non-linear isotropic partial differential equation derived from Fourier's law of heat conduction and law of energy conservation, as shown in Eq. (1):

$$\rho(T)c_p(T)\frac{\partial T}{\partial t}=\frac{\partial}{\partial x}\left(k(T)\frac{\partial T}{\partial x}\right)+\frac{\partial}{\partial y}\left(k(T)\frac{\partial T}{\partial y}\right)+\frac{\partial}{\partial z}\left(k(T)\frac{\partial T}{\partial z}\right)+q \tag{1}$$

where $\rho(T)$, $c_p(T)$ and $k(T)$ are temperature-dependent density, specific heat, and thermal conductivity, respectively. These temperature-dependent thermo-physical properties for S700 were obtained from the literature [41], as shown in Fig. 4. It must be noted that the units are arranged so that all properties can be shown in a single graph. The parent and filler materials share almost the same strength level and thus, in the FE models were defined as identical materials to both the same material properties were assigned.

In Eq. (1), q (W/m^3) is known as the volumetric heat source density or internal heat generation rate. A volumetric heat source with double ellipsoidal distribution proposed by Goldak et al. [36] was considered to represent the energy transferred from the welding arc to the base and weld materials, as shown schematically in Fig. 5. Two heat flux distributions are defined by this model, one for the front half and the other for the rear half of the heat source, as expressed by Eq. (2) and Eq. (3), respectively:

$$q_f(x,y,z,t)=\frac{6\sqrt{3}f_fQ}{ab_fc\pi\sqrt{\pi}}e^{-3\left(\frac{x^2}{a^2}+\frac{[y-vt-y_0]^2}{b_f^2}+\frac{z^2}{c^2}\right)},\quad y\geq 0 \tag{2}$$

$$q_r(x,y,z,t)=\frac{6\sqrt{3}f_rQ}{ab_rc\pi\sqrt{\pi}}e^{-3\left(\frac{x^2}{a^2}+\frac{[y-vt-y_0]^2}{b_r^2}+\frac{z^2}{c^2}\right)},\quad y<0 \tag{3}$$

q_f and q_r are the heat flux distributions accumulated in the front half and rear half of the heat source, respectively. Q is the power of the welding arc, which can be calculated based on the welding current (I), voltage (V) and welding efficiency coefficient (η). The parameters a. b_f, b_r and c are characteristics of the welding heat source. f_f and f_r are dimensionless parameters, and account for the fractions of heat deposited in the front and rear half of the heat source, respectively. Taking the continuity of the heat source into consideration the following relationships are observable:

$$\frac{f_r}{b_r}=\frac{f_f}{b_f} \tag{4}$$

$$f_f+f_r=2 \tag{5}$$

The welding torch in the experiments had a work angle of 45°. Simulation of the moving heat source at a specified angle necessitates transformation of points from the global coordinate system into a local coordinate system by means of rotation and translation. Considering the defined convention for the welding direction, rotations of −45° and 45° were performed for side 1 and side 2, respectively:

$$\begin{bmatrix}x\\y\\z\end{bmatrix}=\begin{bmatrix}\cos45 & 0 & \sin45\\0 & 1 & 0\\-\sin45 & 0 & \cos45\end{bmatrix}\begin{bmatrix}X-X_0\\Y-Y_0\\Z-Z_0\end{bmatrix} \tag{6}$$

$$\begin{bmatrix}x\\y\\z\end{bmatrix}=\begin{bmatrix}\cos45 & 0 & -\sin45\\0 & 1 & 0\\\sin45 & 0 & \cos45\end{bmatrix}\begin{bmatrix}X-X_0\\Y-Y_0\\Z-Z_0\end{bmatrix} \tag{7}$$

where x, y and z represent nodal coordinates in the local coordinate system and X, Y and Z are nodal coordinates in the global coordinate system. Mathematical equations representing the moving heat source were implemented in the ABAQUS user-subroutine DFLUX programmed in FORTRAN. The user-subroutine DFLUX calculated the position of the heat source with respect to time, travel speed of the torch and nodal coordinates. It then, calculated the non-uniform volumetric flux distri-

Table 5
Adjusted heat source parameters.

Parameter	a (mm)	b_f (mm)	b_r (mm)	c (mm)	f_f	f_r
Value	7	3	10	7	0.46	1.54

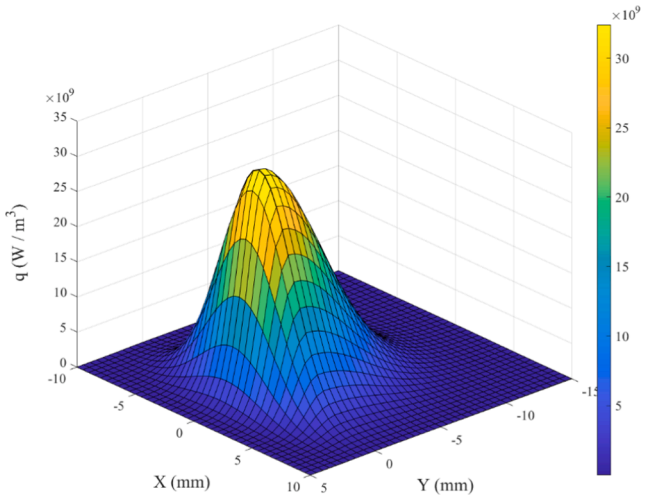

Fig. 6. Power distribution of the double-ellipsoidal heat source using the parameters in Table 5.

bution at each integration point as a function of time, the position of the heat source and using the heat source power.

Temperature histories during the welding must be precisely predicted to be able to have an acceptable accuracy in prediction of residual stresses and strains. To do so, calibration of the heat source is required, which was accomplished by iteration of the Goldak's characteristics of the weld pool so that a close agreement was reached between the nodal temperatures from the simulation and measurements. Matching the boundaries of the FZ and HAZ captured by simulation against the macrograph of the weld cross section was performed as the further calibration of the heat source. Table 5 summarizes the heat source parameters and their adjusted values to calibrate the thermal model. Using the calibrated Goldak's heat source parameters in Table 5, power distribution of the double-ellipsoidal heat source for the front half and rare half of the energy source on the top surface is shown in Fig. 6.

In all the simulation cases, ambient temperature was set to 20 °C. To reach a unique solution for Eq. (1), it should be solved subject to specific boundary conditions. In welding simulation problems, the most widely applied thermal boundary conditions are the heat loss due to convection and radiation from free surfaces of the specimen to the surroundings, as depicted schematically in Fig. 7. Heat loss by convection during welding is generally taken into account using Newton's law of cooling and heat loss by radiation is modeled by applying Stefan-Boltzmann's law. An alternative method to model the heat loss during welding is to account for the combined effect of convection and radiation, which is generally performed by defining a temperature-dependent heat transfer coefficient [42,43], as is expressed by the following equation:

$$h = \begin{cases} 0.0668 \times T\left(\dfrac{W}{m^{2^\circ}C}\right) & 0 \le T \le 500 \\ 0.231 \times T - 82.1\left(\dfrac{W}{m^{2^\circ}C}\right) & T \ge 500 \end{cases} \tag{8}$$

where T(°C) is temperature and h denotes the temperature-dependent heat transfer coefficient. The mathematical expressions presented in Eq. (8) were implemented in the user-subroutine FILM to model the combined thermal boundary conditions. It should be noted that heat transfer by means of conduction between the specimen and clamping are ignored since the distance between the heat source and clamped areas are large enough so that the temperature rise at those regions are negligible.

The interaction between solid and liquid phases is not included in the ABAQUS package and modeling the fluid flow is not directly possible when using this FE software. However, since this phenomenon has consequential influence on the temperature distribution of the weld pool, it was accounted for using artificially increased thermal conductivity at temperatures higher than the melting point, i.e., thermal conductivity at temperatures higher than the liquidus temperature was considered almost 4 times as large as that value at room temperature. To account for the thermal effects of solidification in the weld pool, the latent heat of fusion was considered with a value of 270×10^3 J/kg between the solidus temperature of 1430 °C and liquidus temperature of 1480 °C.

3.3. Mechanical analysis

In each mechanical analysis, the temperature histories predicted by the corresponding thermal analysis were transferred and applied as an input (thermal load) in a non-linear elastic-plastic analysis to calculate the residual stresses and distortions. In the current study, the strain rate due creep was not taken into account in the mechanical analysis since in the entire thermal cycle, the time period with high temperature was limited to a few seconds and the effect of creep on the total strain was insignificant [21,25]. Phase transformation in solid state is one of the phenomena which may have significant effect on welding-induced stresses and strains depending on the type of material. Austenitic stainless steels are known not to experience phase transformation [9] while carbon steels are more prone to phase transformation. In this regard, welding-induced residual stress and distortion in medium and high carbon steels are stated to be more significantly affected by phase transformation than low carbon steels [11,13]. Ferro et al. [44], however, found that including solid state phase transformation in mechanical analysis in low carbon steels results in more accurate and reliable values for residual notch stress intensity factors. In this study, due to lack

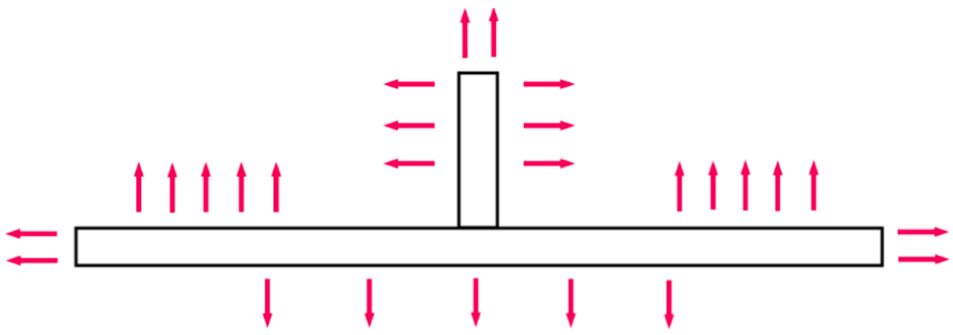

Fig. 7. Illustration of the heat loss by means of convection and radiation from the free surfaces of the T-joints.

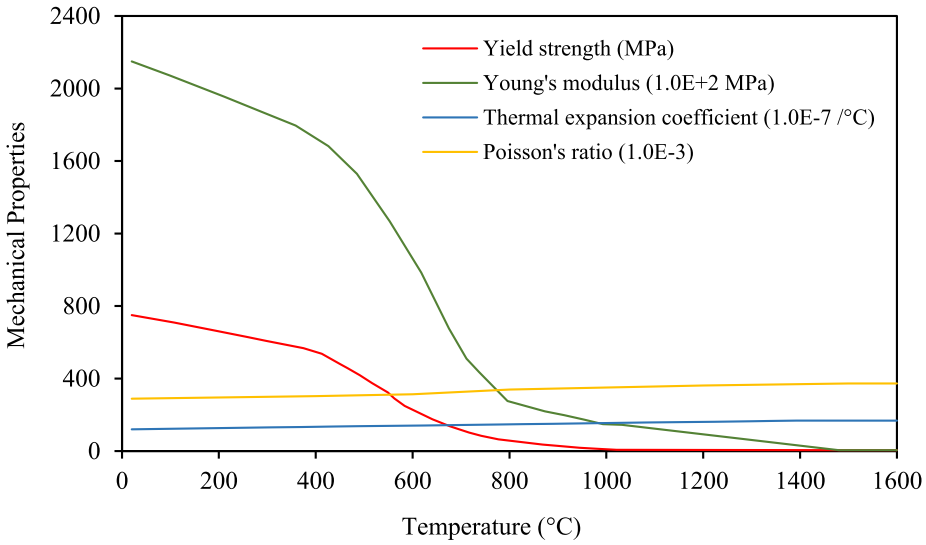

Fig. 8. Temperature-dependent mechanical properties of S700.

of experimental data being essential to include phase transformation, strain rate due to phase change was not included the mechanical analysis. Nevertheless, the influence of phase change on formation of residual stresses and strains in HSSs is of interest and a further study would include such effect. Excluding the strain rate components due to phase transformation and creep, the total strain rate is decomposed by its constituents as follows:

$$\{d\varepsilon^{total}\} = \{d\varepsilon^{e}\} + \{d\varepsilon^{p}\} + \{d\varepsilon^{th}\} \tag{9}$$

where $d\varepsilon^{total}$ is the increment of total strain. $d\varepsilon^{e}$, $d\varepsilon^{p}$ and $d\varepsilon^{th}$ correspond to elastic, plastic, and thermal strain increments, respectively. Elastic strain was modeled based on the isotropic Hooke's law using temperature-dependent modulus of elasticity and Poisson's ratio. Modeling the plastic strain component was accomplished using a rate-independent plastic model including the following features: Von Mises yield criterion, isotropic strain hardening law and temperature-dependent mechanical properties. A temperature-dependent thermal expansion coefficient was used in modeling of the thermal strain. Temperature-dependent mechanical properties used in calculation of the structural response were taken from the literature [41], as presented in Fig. 8.

In the mechanical analysis, the effect of annealing on strain hardening was considered by defining an annealing temperature. If the temperature of any material point rises above the annealing temperature, strain hardening memory is lost by resetting the equivalent plastic strain to zero at that material point. On condition that the temperature of a material point falls below the defined annealing temperature during cooling, material retrieves its work hardening memory at that point. In this study, the annealing temperature was set to 900 °C [16].

In welded joints, application of welding fixtures or clamps is one of the major techniques to control the induced distortions. Using fixtures in over-restraint conditions, can reduce the welding deformation, it can, however, negatively affect residual stress fields where stresses can build up and cause cracking problems. In welding of under-constrained components, the development of distortions can increase dimensional instability. Although in the case of short fillet welds, smaller levels of distortion are expected compared to the continuous welding, the residual stress field should be considered carefully. In this regard, correct application of external restraints contributes to optimization of welding-induced stresses and strains. Regarding tack welds (temporary non-continuous welds), although by applying the main weld layer, stress fields due to applying the tack welds are mainly annihilated, welding deformations caused by those tack welds will remain and must thus be thoroughly taken into consideration. This matter, in real applications such as robotized welding is of particular importance where the accuracy and productivity of such technologies may decline if the previous deformations due to tack welds are not accounted for. In the experimental part of the study, two clamping conditions were tested; In one case, the external constraints were applied in such a way that the related specimen was restrained at one end in a specified area. In the corresponding FE model, the mechanical boundary conditions were applied to simulate the clamping condition, and all the nodes in the specified area were restricted to move translationally and rotationally, as shown in Fig. 9 (a). The other clamping configuration was considered to fix the specimen rigidly at both ends in the two defined areas. In the related FE model, all the nodes in those areas were prevented from rotation and translation, as shown in Fig. 9 (b). It should be noted that the length of the clamping in the X-direction was 100 mm. After welding and reaching the ambient temperature, the mechanical boundary conditions were defined in the FE models corresponding to the removal of the clamps. That is, after the cooling stage, all the mechanical boundary conditions were deactivated and those to prevent the rigid body motion only were defined, as shown in Fig. 9 (c).

4. Results and discussion

4.1. Results of thermal simulation

The temperature distribution and peak temperature captured by the FE thermal simulation of short fillet welds in T-joints made of S700 are shown in Fig. 10. It should be noted that due to the identical welding parameters and heat source model for all the cases, the thermal analysis results are presented only for one of the cases (FS1). As can be seen in Fig. 10, the maximum temperature of the weld pool is approximately 1800 °C. In the same figure, the FZ, i.e., the regions with peak temperatures higher than the liquidus temperature (1480 °C) are shown in light gray. To achieve reasonable results for mechanical response, an accurate prediction of temperature distribution during the welding is a requirement.

Matching the shape and size of the weld pool from the simulation and experimental measurements is one of the indices to evaluate the correctness of temperature distribution during the welding. Fig. 11 represents the depth of penetration captured from the macrograph of the weld cross section versus the simulation at a distance of 5 mm from the start of the segment. As shown in Fig. 11, the depth of penetration is well-captured by simulation and boundaries of the FZ from the simulation

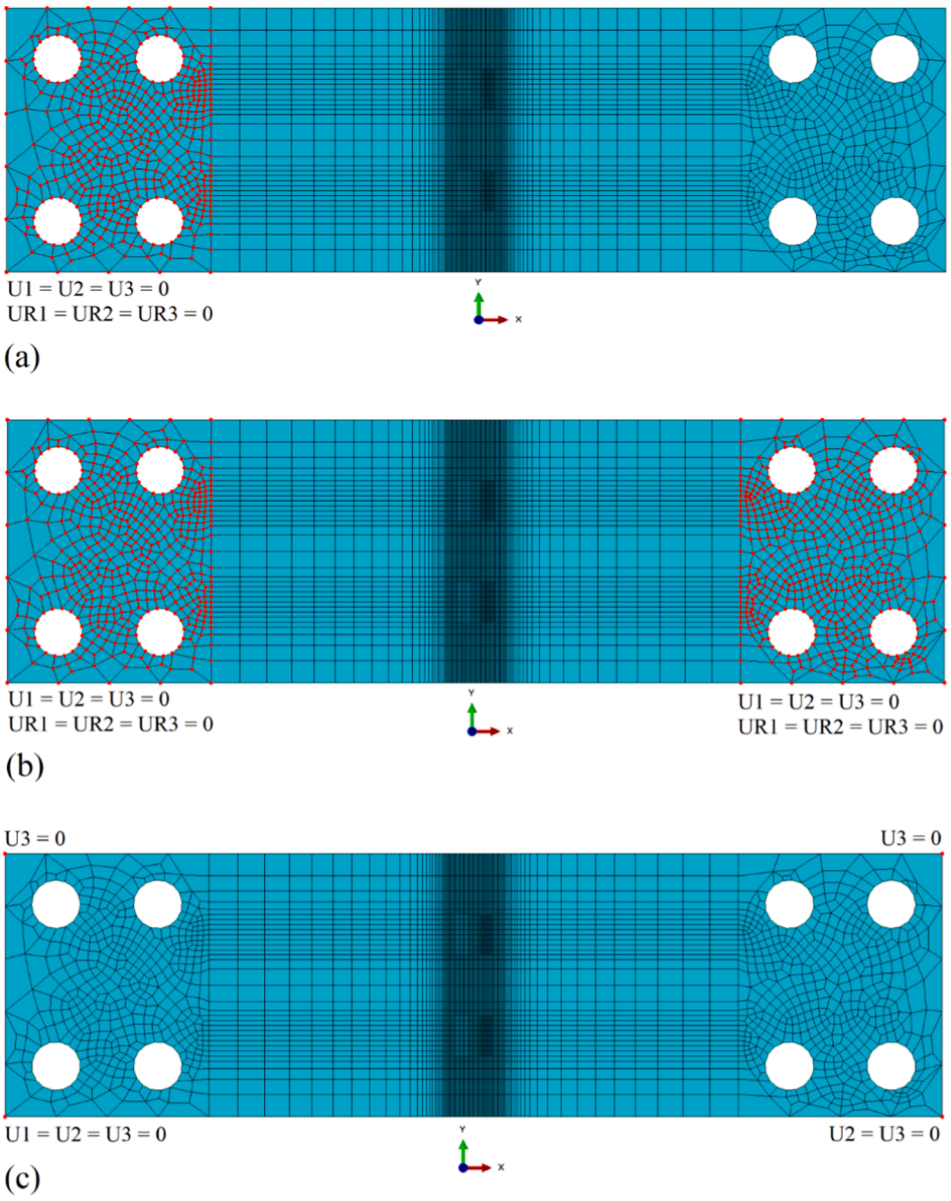

Fig. 9. Representation of the mechanical boundary conditions assigned to the FE models for: (a) clamping at one end; (b) clamping at both ends; and (c) removal of the clamps.

reasonably match the macrograph of the weld cross section. Matching the experimental and simulated temperature histories, which was carried out by adjusting the heat source parameters and calibration of the heat loss model, is another index of the accuracy of thermal analysis. In this respect, the experimental time-temperature curves obtained through the thermocouple measurements at several locations and the simulation results for the corresponding nodes are presented in Fig. 12. As mentioned before, the applied heat input and specimen configuration for all the cases were identical and hence, only one of the specimens (FS1) was chosen for the sake of comparison in terms of the experimental and simulated thermal cycles.

For a better clarity regarding the features of time-temperature curves, the entire temperature histories obtained from the simulation and those captured by the thermocouple measurements for FS1 are divided into four parts (a–d), as shown in Fig. 12. That is, Fig. 12 (a–d), refers to the welding thermal cycles of segments W1–W4, respectively. In Fig. 12, T1–T4 are the thermocouples attached on the top surface of the specimen (specified in Fig. 2), and X1–X4 refer to the distances of those thermocouples from the weld toes and the corresponding nodal distances in the FE model. X1–X4, were measured from the 3D scan image of the specimen post welding and after detaching the thermocouples. It can be seen that the simulated curves are in close concurrence with the experimental ones in terms of the heating and cooling rates, and the peak temperatures. Such agreement implies that the heat source parameters (Goldak's characteristics) were adjusted reasonably, and the heat loss model was calibrated correctly. Comparing the numerical results of T1 in Fig. 12 (a) to T2 in Fig. 12 (b), with the specified distances of 1.25 and 4 mm from the heat source, respectively, shows that the regions close to the weld, experienced considerably higher peak temperatures compared to the areas farther from the heat source, while reasonably maintained the heating rates similar to those areas. Based on the results of thermal analysis, it was assumed that the thermal FE model validated through the transient temperature histories and the weld pool dimensions, was accurate enough in order to transfer the nodal temperatures from the thermal to the mechanical model.

It is expected that welds with shorter lengths experience faster cooling rates. In this regard, a comparison is drawn to clarify how the cooling rate changes for the fillet welds with considerably shorter

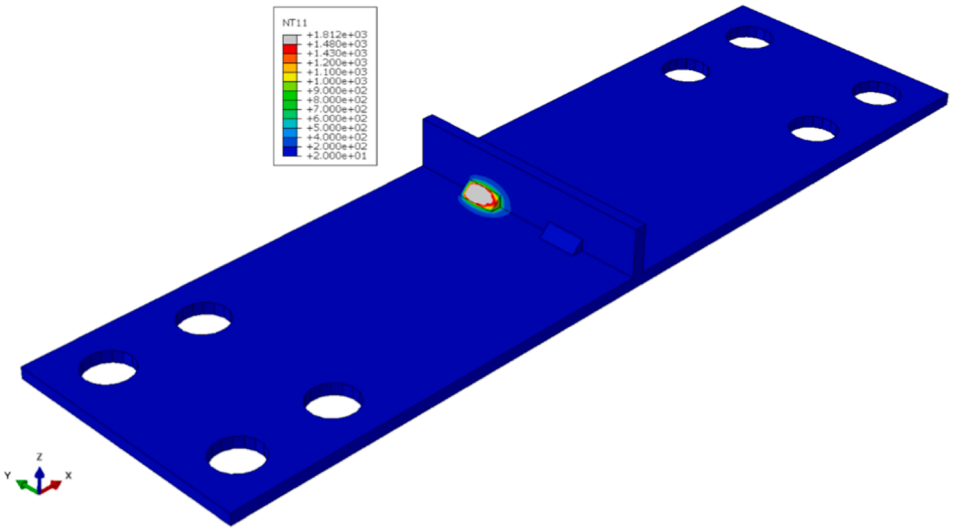

Fig. 10. Temperature contours captured during the welding of W2 on FS1.

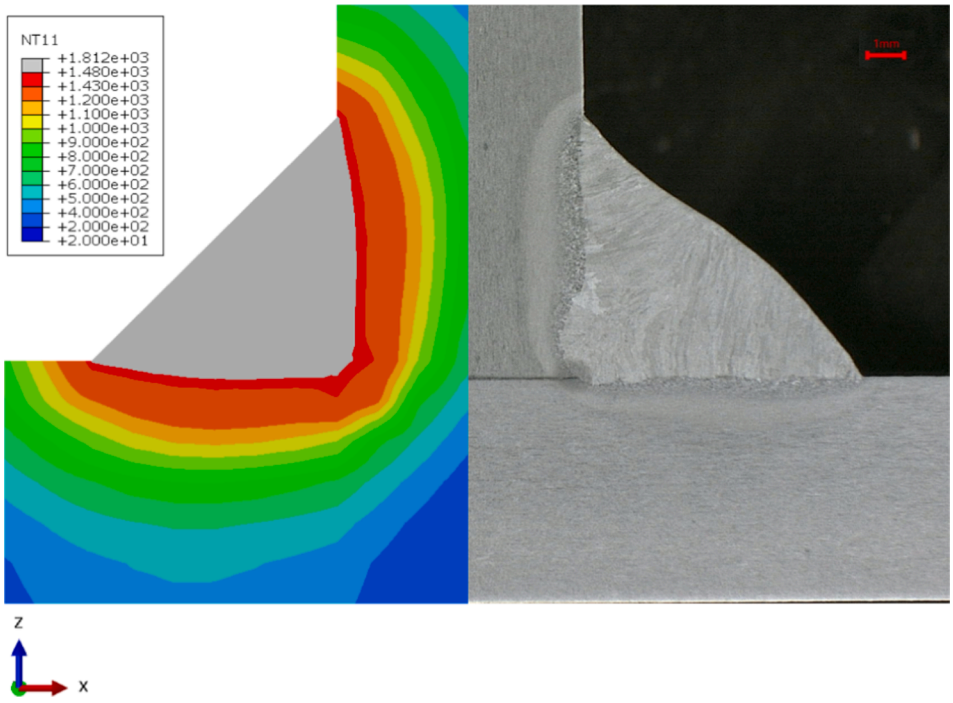

Fig. 11. Welding temperatures (NT11) and Boundaries of the weld pool from the simulation versus the experiment through the thickness.

lengths compared to the continuous ones. In addition to the FE simulation of short fillet welds with a specified length of 20 mm, an FE thermal simulation for a double-sided fillet weld with an approximate length of 122 mm on each side, was performed. It should be noted that identical heat inputs for both cases were used. Fig. 13 shows the time-temperature curves captured from the simulation for a node positioned at a distance of X = 0.5 mm from the weld toe at half-length of the weld in each case. As can be seen, while both welds experienced almost the same peak temperature and heating rate, a considerable difference was obtained for the cooling rate. From Fig. 13, cooling times ($t_{8/5} = t_{500} - t_{800}$), for the continuous and short welds, are 11.45 and 3.86 s, respectively. The calculated cooling rates ($\nu_{8/5} = 300/(t_{8/5})$) are 26.2 and 77.7 °C/s, for the continuous and short welds, respectively.

This heating and very fast cooling due to the short length of the weld can produce localized residual stress fields with large magnitudes. In addition, $t_{8/5}$ is known to have a significant effect on the final microstructure of the HAZ in welded structures since most microstructural changes occur at temperatures above 500 °C. As $t_{8/5}$ decreases, the tendency to form martensite increases, and, consequently, the hardness of the HAZ rises. In direct-quenched HSSs and UHSSs, the maximum limit of $t_{8/5}$ should not be exceeded to avoid detrimental softening in the HAZ [45,46]. Microstructural investigation is out of the scope of the current study, it is, however, important to note that the FE thermal simulation can contribute to conduct comparative studies on the effect of cooling rate due to the different weld lengths or heat inputs on the microstructure and mechanical properties of the advanced HSSs.

4.2. The simulated residual stresses and angular distortion

The effect of external constraints and welding sequence on

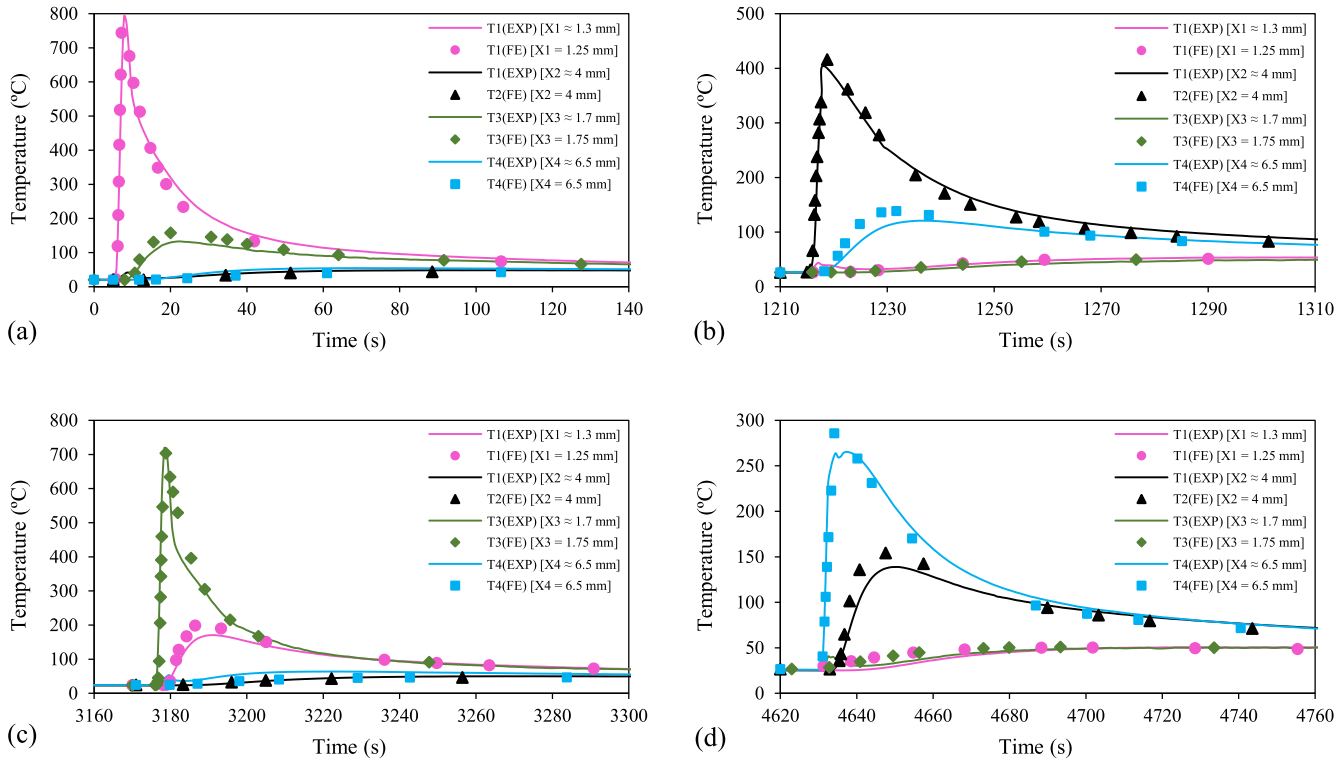

Fig. 12. The experimental versus simulated thermal cycles for FS1 during the welding of segments: (a) W1; (b) W2; (c) W3; and (d) W4.

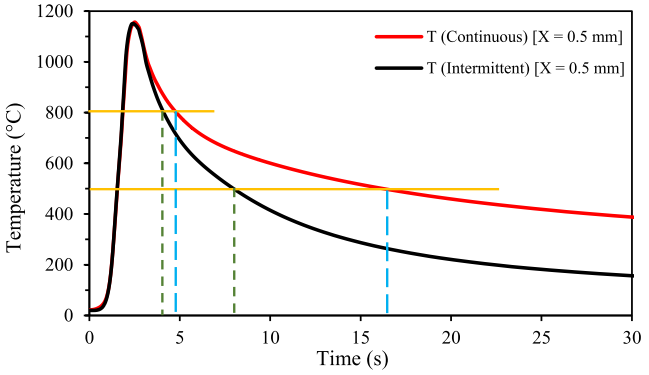

Fig. 13. Comparison of the simulated thermal cycles for a short fillet weld with a length of 20 mm, and a continuous fillet weld with a length of 122 mm.

development of residual stresses and angular distortion, which is induced by non-uniform heating and cooling during the welding, was investigated. Experimental measurements were conducted to verify the results of the simulated residual stresses and angular distortion regarding the distribution patterns and magnitudes due to change in the mechanical boundary conditions and welding sequence.

Measurement of angular distortion was fulfilled by using a 3D scanner before welding (for possible small deformation), and after the deposition of each fillet weld and reaching the ambient temperature for each case. Angular distortion was measured in the mid-section (half-way along the weld line) and in the transverse direction (perpendicular to the weld line) at the bottom side of the specimen (Path 5), as shown schematically in Fig. 14.

Transverse surface residual stresses on the top surface of FS1 and CS1 were measured at the mid-length of W1 (Path 1) and W4 (Path 4) to validate the simulation results using XRD by a Stresstech X3000 G3 device with a collimator diameter of 1 mm. The developed residual stresses for the other cases, and residual stresses along path 2 and path 3, were studied from the results of the validated simulations.

4.2.1. *Angular distortion*

Contours of angular distortion for FS1 and FS2 after removal of the clamps are shown in Fig. 15 (a) and 15 (b), respectively. Those for CS1 and CS2 after release from the external constraints are depicted in Fig. 16 (a) and 16 (b). As can be observed, the patterns of angular distortion (deflection in the Z-direction) for all the welding cases are similar. Through the comparison between Fig. 15 (a) and 16 (a), and Fig. 15 (b) and 16 (b), it can be understood that the external constraints at both ends slightly better prevented angular distortion compared to the clamping at one end after these constraints were removed.

In order to evaluate the accuracy of the FE simulations with regard to the effect of welding sequence and external restraints on angular distortion quantitatively, the sequential and cumulative angular distortions for FS1 and FS2 from the simulations and measurements (See Fig. 14 for the measurement path) are compared. For CS1 and CS2, due to the very small sequential distortions expected after each short weld (W1–W4), only the final angular distortions (after removal of the clamps) were measured experimentally, and the sequential distortions are discussed based on the numerical results. The results of the sequential angular distortions for FS1 and FS2 are shown in Fig. 17 (a) and (b), respectively. The simulated data are plotted with solid lines, while the measurement data are shown with circular marks. The simulated sequential angular distortions for CS1 and CS2, before release from the clamps are shown in Fig. 18 (a) and (b), respectively.

As can be seen in Fig. 17 (a) and (b), the distortion predictions by FE simulations are in reasonable agreements with the measurements. In almost all the cases, simulation overpredicts the angular distortion when compared to the experimental measurements. Both the simulation and measurement demonstrate that the final angular distortion produced in FS1 is slightly greater than that induced in FS2. For FS1, the experimental and simulated values are 3.95 and 4.61 mm, respectively, which makes a percent error of 16.7 %. In the same vein, the experimental and numerical values obtained for FS2 are 3.76 and 4.34 mm with a percent

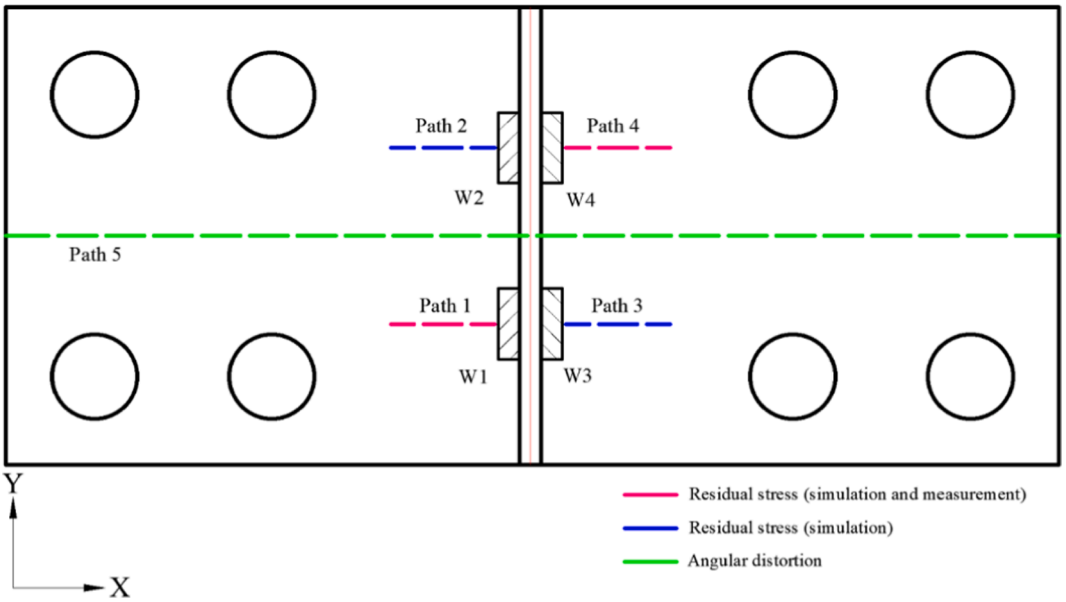

Fig. 14. Illustration of the measurement paths for angular distortion at the bottom surface, and residual stresses on the top surface.

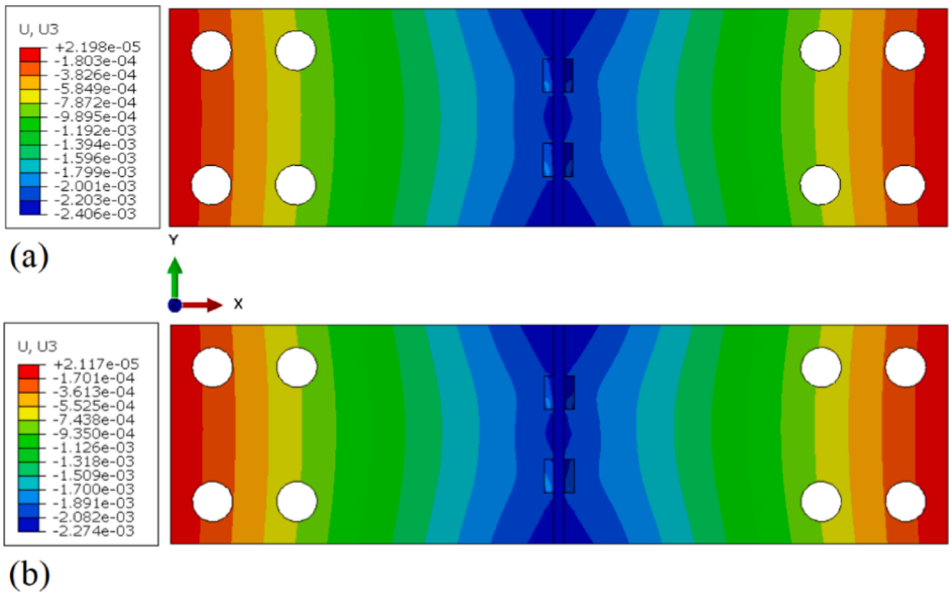

Fig. 15. Contours of the final angular distortion for: (a) FS1; and (b) FS2 (Units are in m).

error of 15.4 %. The final angular distortion in FS1 is approximately 6 % (from both the simulation and measurements) greater than that of FS2. Compared to the size of the specimen and final angular distortion, the difference is minor. Nevertheless, in practice where a large number of short fillet welds are required (based on the design), the difference due to a change in the welding sequence can be considerable. The same trend, i.e., a slightly greater angular distortion due to the welding sequence S1 compared to S2, can be seen in Fig. 18 (a) and (b). The simulated angular distortions for CS1 and CS2 in the clamped conditions are 0.51 and 0.48 mm, respectively. The angular distortion specific to each fillet weld (W1–W4) from the simulation and measurements for FS1 and FS2 are compared in Fig. 19 (a). The simulated angular distortions due to the deposition of the fillet welds (W1–W4) for CS1 and CS2 are shown in Fig. 19 (b). It should be noted that the values in Fig. 19 (b) refer to the situation when CS1 and CS2 were still in clamps. It can be seen in Fig. 19 (a), as was predicted by simulation and measurements, in both FS1 or FS2, W2 and W3, have the largest and the smallest shares in the final angular distortion, respectively. The same trend respecting the shares of W2 and W3 in the total angular distortion, can be observed for CS1 and CS2 in the restrained conditions in Fig. 19 (b).

The effect of external constraints on the angular distortions induced in the studied cases, are evaluated by plotting the simulated angular distortions after removal of the clamps, as shown in Fig. 20. As was expected, clamping the specimen at one end permitted the development of angular distortion freely during the welding, and, therefore, releasing the related specimens after reaching the ambient temperature had no effect on the magnitude of the maximum angular distortion. For a higher degree of geometrical constraints, as experienced by CS1 and CS2, deformation is prevented during the welding by increasing plastic strains and reducing elastic strains. Elastic strains or locked-in stresses are responsible for the deformations after unclamping [17]. As the external constraints were removed, the remaining elastic strains were released partially as the specimen started to deform. As can be seen in Fig. 20, the smallest deformation obtained for the specimen which was

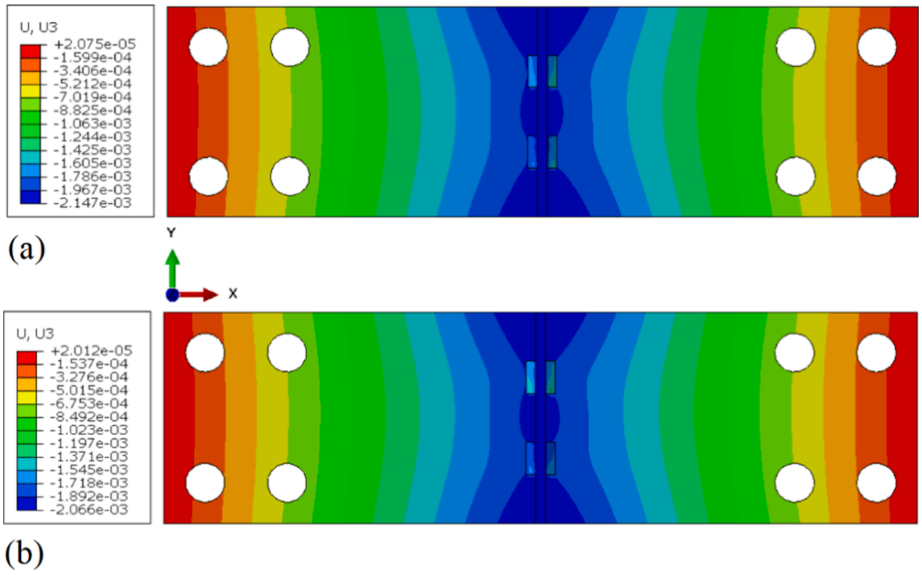

Fig. 16. Contours of the final angular distortion for: (a) CS1; and (b) CS2 (Units are in m).

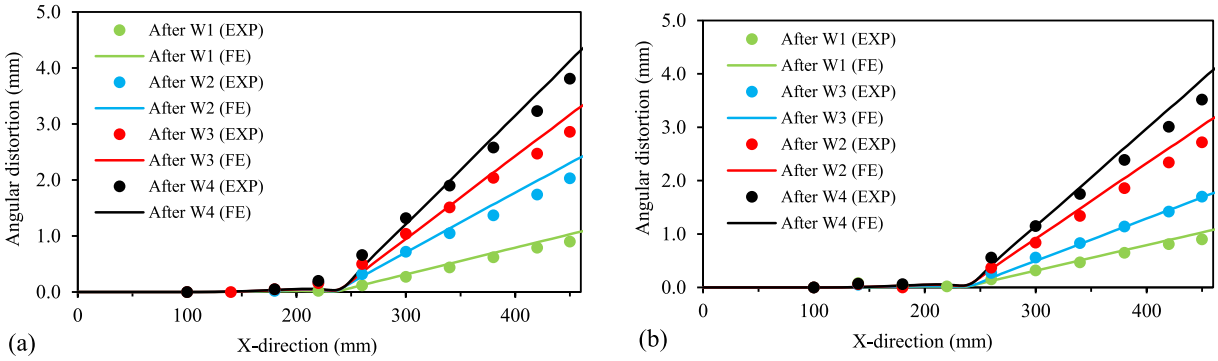

Fig. 17. The simulated versus the measured sequential angular distortions for: (a) FS1; and (b) FS2.

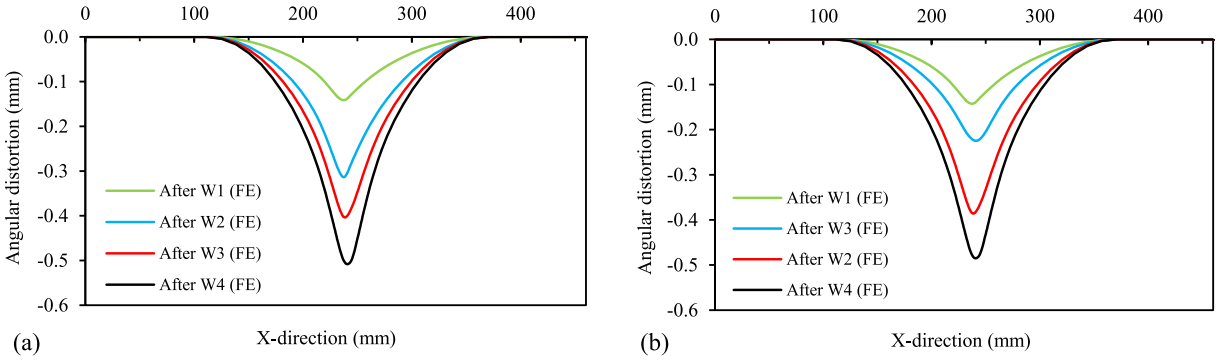

Fig. 18. The simulated sequential angular distortions in the restrained condition for: (a) CS1; and (b) CS2.

welded using sequence S2 and was clamped at both ends, while the largest angular distortion captured for the specimen being clamped only at one end and was welded using sequence S1. The results of simulations show that the angular distortion for FS1 is 9.2 % greater than that of CS1. In the same manner, the angular distortion for FS2 is 7.1 % larger than that for CS2. Based on the distortions due to the different welding sequences and external restraints, it can be understood that for this specimen configuration with a specified number of short fillet welds with a length of 20 mm each, the effect of the welding sequence is slightly smaller than that of the external constraints.

In order to compare the effect of clamping on angular distortion when short fillet weld changes to continuous fillet weld, for a similar specimen, a thermal simulation was performed. The simulation included deposition of the weld metal on both sides of the T-joint specimen in the same direction and with the same heat input being applied to the other cases in this study. The weld length on each side was approximately 122 mm. In the subsequent mechanical analyses, the two boundary conditions, which were previously used for the other welding cases, were applied. The results of the angular distortion after reaching the ambient temperature, before and after unclamping for the continuous and short

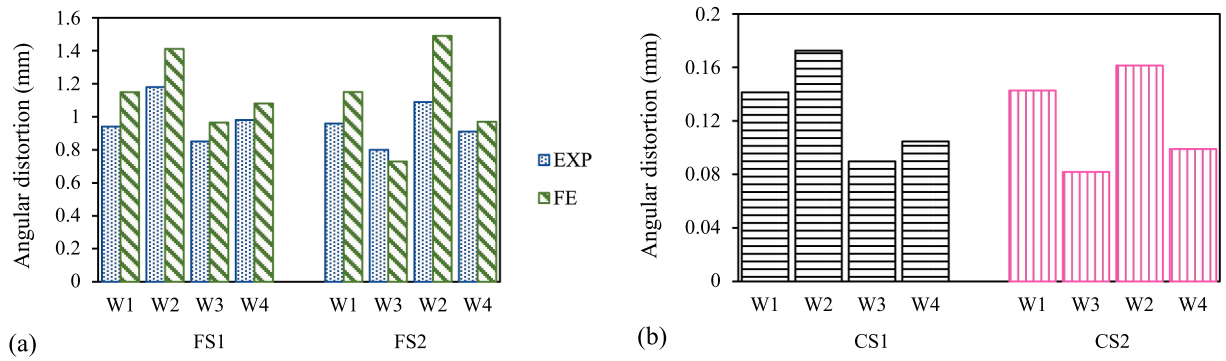

Fig. 19. The angular distortions developed due to each fillet weld: (a) from the simulation and measurements for FS1 and FS2; (b) from the simulation for CS1 and CS2.

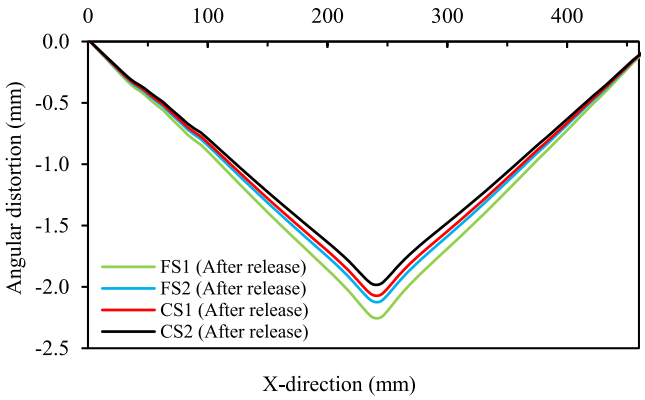

Fig. 20. The final angular distortions after unclamping of the specimens.

welds are shown in Fig. 21.

As can be seen in Fig. 21, in the case of continuous fillet welds, using higher degree external constraints could considerably reduce the final distortion by increasing plastic strain and reducing the remaining elastic strains. In the case of short fillet welds, however, adding more restraints, only slightly improved the distortion prevention. It can be understood that in the case of short fillet welds, adding more rigidity does not considerably reduce the angular distortion, and other distortion control techniques, such as applying pre-deformation can thus be considered.

4.2.2. *Transverse residual stress*

In the current study, transverse residual stresses for FS1 and CS1 along the specified paths (see Fig. 14) were measured to validate the corresponding simulation results. The rest of the comparisons are drawn based on the validated FE models. The stress measurement paths on the top surface start at approximately 1 mm from the weld toe and are extended in the X-direction (almost 25 mm in length). It should be noted that in comparisons of residual stresses, path 1 and path 2 are considered in the negative direction of the X-axis, while path 3 and path 4 are shown in the positive direction of the X-axis. Fig. 22 shows the measured and simulated transverse stresses for FS1 after cooling down to ambient temperature. As can be seen in Fig. 22, the simulation results are in a relatively good agreement with the measurement data. It should be noted that XRD measurement data always fall within an error band which can be considerable in the FZ and HAZ and hence, the issue should be taken into account when comparing with simulation results. As moving from the weld toe in the X-direction, there exist regions of maximum tensile residual stress in the HAZ at 3–4 mm from the weld toes predicted by experimental measurements and simulation. Passing through the HAZ, the tensile residual stresses fall in magnitude rapidly. As clearly shown in Fig. 22, based on both the simulation and measurements, the peak tensile transverse stress due to the welding of W4 is considerably greater than that of W1. The measurement data demonstrate that the maximum tensile transverse stress due to W4 almost reaches the yield strength of the base material, while the peak residual stress predicted by simulation exceeds the yield strength of the base

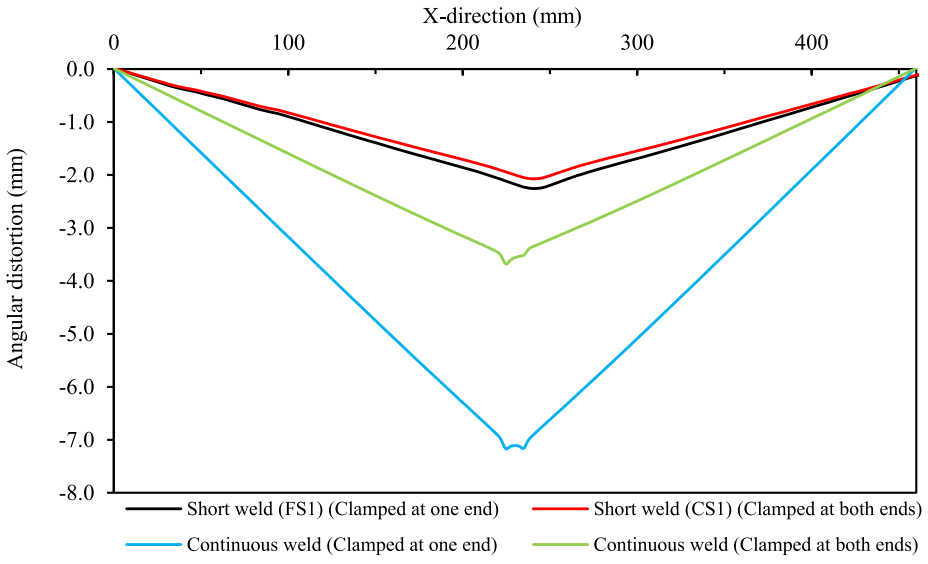

Fig. 21. The simulated final angular distortions for the cases with continuous welds and short fillet welds (FS1 and CS1).

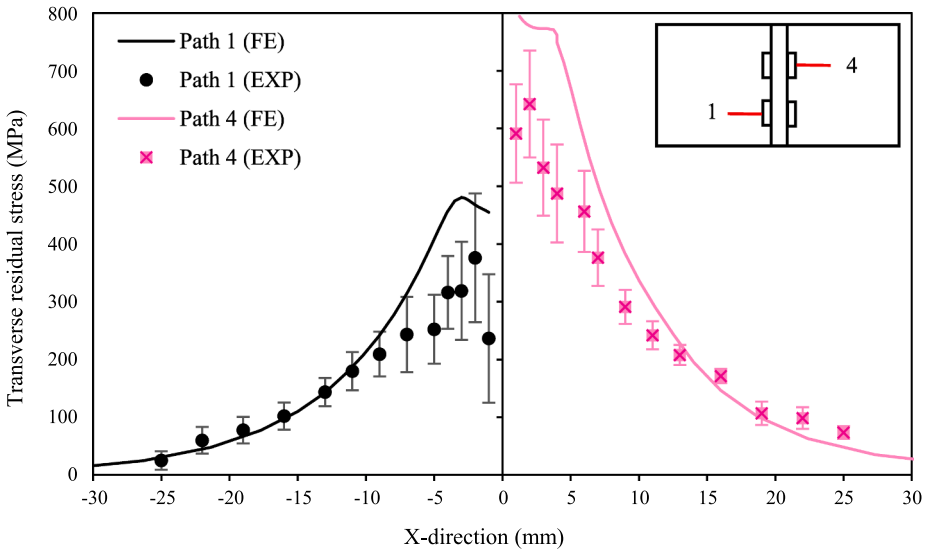

Fig. 22. Comparison of the measured and simulated transverse residual stresses for FS1 along path 1 and path 4.

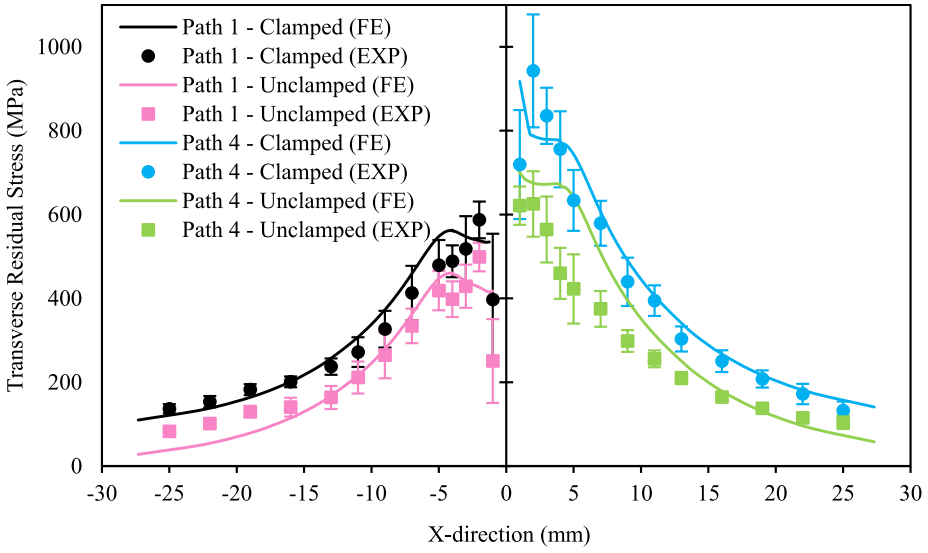

Fig. 23. Comparison of the measured and simulated transverse residual stresses for CS1 along path 1 and path 4, before and after unclamping.

plate slightly. For W1, the maximum tensile residual stress from both the simulation and measurement is approximately 480 MPa, which is almost 65 % of the yield strength of the base material.

In order to validate the results of the simulation regarding the effect of external constraints on the residual stress fields, the transverse residual stresses before and after removal of the external restraints for CS1 were measured and compared with those of the corresponding simulation, as shown in Fig. 23. As is observable in Fig. 23, the simulation results are in a relatively good agreement with the experimental data in terms of both the trend and peak magnitudes, before and after removal of the constraints. Along both paths, after removal of the constraints, tensile transverse stress fell in value. That is, the approximate peak tensile stress of 560 MPa in the clamped condition decreased to 480 MPa after unclamping for path 1. Along path 4, before removal of the constraints, the maximum tensile transverse stress can exceed 1000 MPa, which is considerably greater than the yield strength of the material. This matter is very important in practice such as intermittently fillet welded connections, where the joint must be welded in strict restraints and perform its service in the permanent external constraints. After removal of the clamps, however, the peak value decreased to yield strength of the material. In this case, similar to FS1, the peak stress along path 4 is considerably greater than that of path 1, both before and after removal of the clamps.

The simulated transverse residual stresses along paths 1–4 for FS1 and FS2 are plotted in Fig. 24 to evaluate the residual stresses induced in the specimens due to each of the fillet welds W1–W4. The simulated transverse stresses for CS1 and CS2 in the clamped and unclamped conditions are shown in Fig. 25 (a) and Fig. 25 (b), respectively. As can be observed in Fig. 24, the residual stress field developed due to W1, has the lowest peak magnitude amongst the others, while the stress field resulting from the deposition of W4 experienced the greatest peak stress for both FS1 and FS2. In FS2, where W3 was deposited on side 2 before W2 on side 1, the peak magnitude in the stress field due to W3 is almost 55 MPa smaller than that in FS1. The peak value in the stress field due to W2 is approximately 75 MPa larger than that in FS1. The maximum tensile transverse stresses in FS2 along path 2 and path 3 are 529 and 680 MPa, respectively.

As can be seen in Fig. 25 (a) and (b), unclamping lowered the levels of transverse stress in an approximate range of 100–120 MPa for both CS1 and CS2, while it retained the distribution patterns similar to the

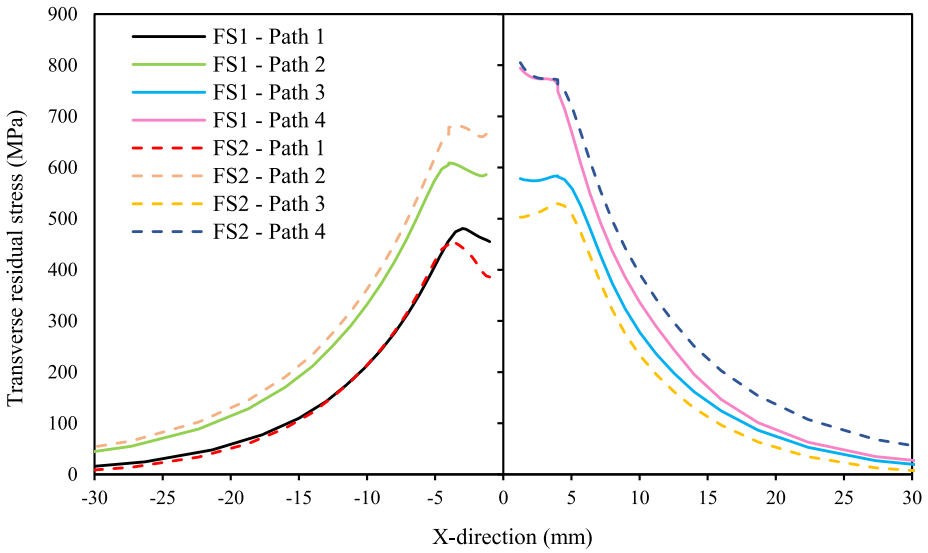

Fig. 24. The simulated transverse residual stresses for FS1 and FS2 along paths 1–4.

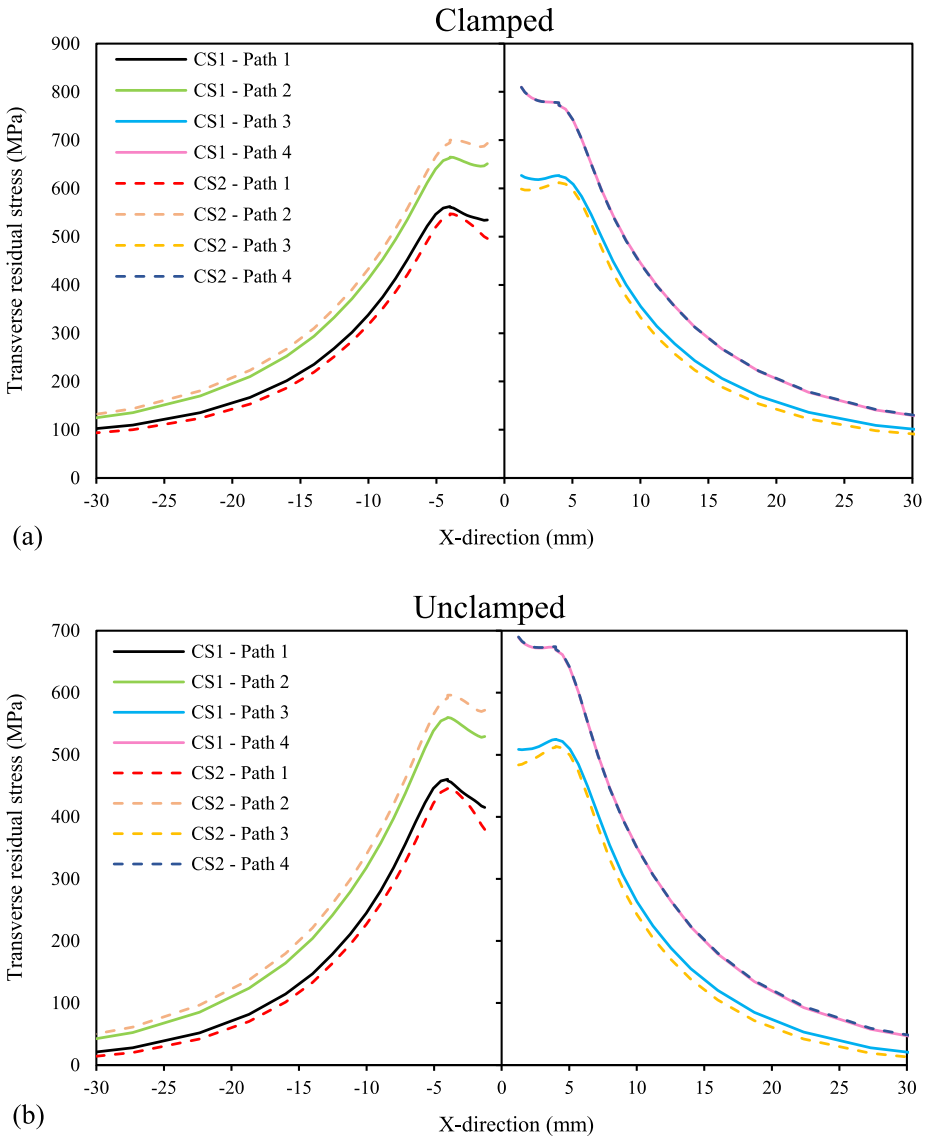

Fig. 25. The simulated transverse residual stresses for CS1 and CS2 along paths 1–4 for: (a) clamped; and (b) unclamped conditions.

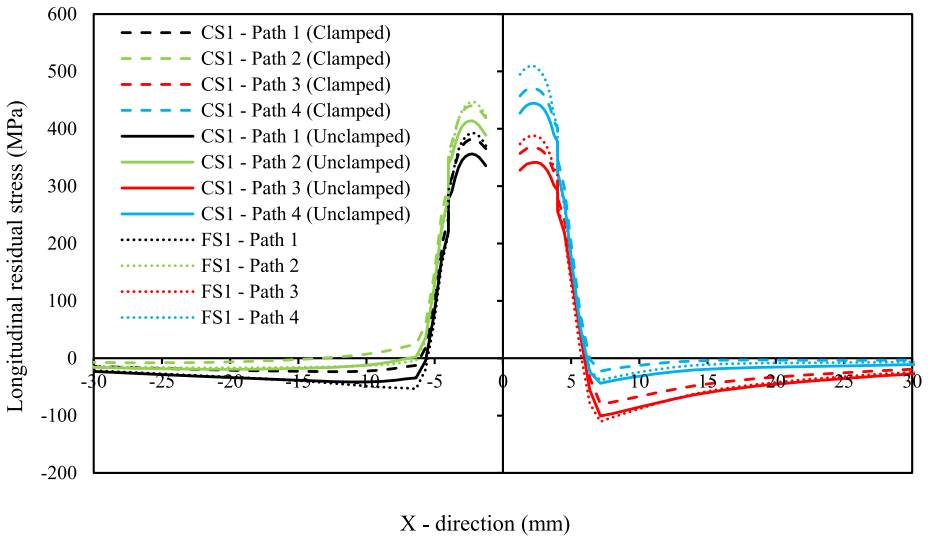

Fig. 26. The simulated longitudinal residual stresses for FS1 and CS1 starting at 1 mm from the weld toe along paths 1–4.

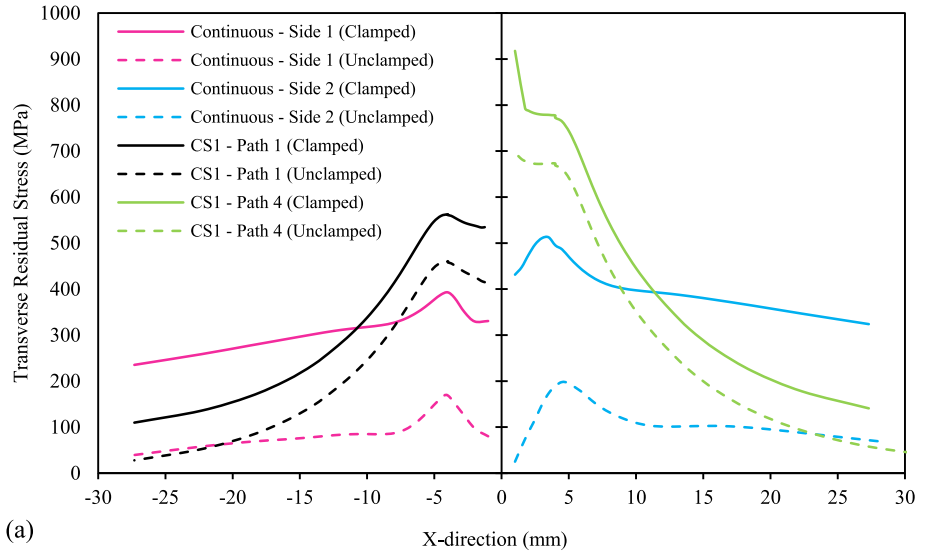

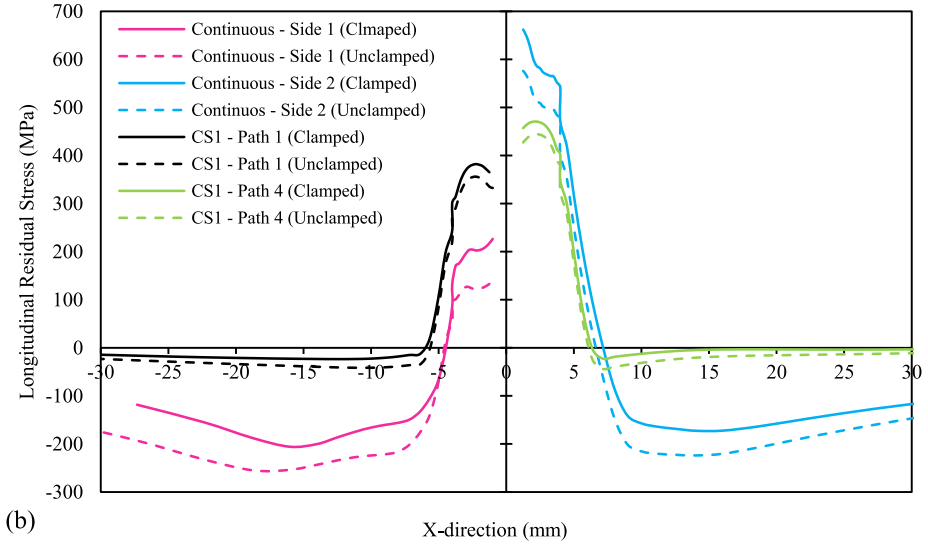

Fig. 27. Comparison between the cases with short and continuous fillet welds (rigidly clamped at both ends) in terms of: (a) Transverse stresses; and (b) longitudinal stresses.

clamped condition. In a comparison between CS1 and CS2, as can be seen, in CS1, the distribution of stress along path 1 has a slightly larger peak magnitude compared to that of CS2. In contrast to S1, when S2 was used, the peak stress along path 3 dropped from 525 to 511 MPa, while the peak magnitude along path 2, rose from 560 to 595 MPa. The distribution of transverse stress along path 4 for both CS1 and CS2 are almost identical.

4.2.3. Longitudinal residual stress

The effect of clamping configuration on longitudinal residual stress was investigated by comparing the simulated longitudinal stress distributions for FS1 and CS1. As shown in Fig. 26, the maximum tensile longitudinal stress, which developed along path 4, is smaller than the maximum transverse stress (see Figs. 24 and 25 (a)) developed along the same path for both FS1 and CS1. As can be seen in Fig. 26, the rigid clamping at both ends produced stresses which were 35–60 MPa smaller compared to the clamping at one end when the specimen was released. The peak longitudinal stresses developed in FS1 along paths 1 and 2 are almost identical to those developed in the clamped CS1 along the same paths. Along path 3 and path 4, the stresses in FS1 were slightly greater than those in CS1 along the same paths. A comparison between the results plotted in Figs. 24 and 25 (a) with those in Fig. 26, indicates that in contrast to the longitudinal stress, the transverse one is more sensitive to the stiffness of the external constraints.

The simulated transverse and longitudinal stresses in one of the cases, CS1 as an example, are compared with those in a double-sided fillet welded T-joint with the similar welding parameters and mechanical boundary conditions. The length of the deposited filler material on each side of the continuous fillet weld case was approximately 122 mm. For CS1, the transverse residual stresses are plotted along paths 1 and 4, and for the continuous case, the stresses are plotted along the two paths perpendicular to the welding direction in the mid-section of the specimen on the top surface on side 1 and side 2, as shown in Fig. 27 (a). In the same vein, the longitudinal stresses are plotted in Fig. 27 (b). Regarding the rigid clamping at both ends, which implies a high restraining stiffness, as can be seen in Fig. 27 (a), transverse residual stresses being induced in the continuous fillet weld case are more sensitive to unclamping than those in the short fillet weld case. That is, after removal of the clamps, release of the transverse residual stresses in the continuous fillet weld case are more considerable than the other case. The peak magnitudes of tensile transverse stresses and the gradient of decrease as moving away from the weld toe, in both the clamped and unclamped conditions, for the short filet welds are significantly greater than those for the continuous case, which indicates the localized stress fields with larger peak magnitudes near the short fillet welds.

As can be seen in Fig. 27 (b), with using high degree mechanical boundary conditions, longitudinal stress of the continuous fillet weld case is more sensitive to the removal of the clamps compared to the short fillet weld case. Longitudinal stress, however, is less sensitive to the removal of the rigid clamps at both ends, compared to transverse stress. The fall of the longitudinal stresses as moving away from the HAZ, for both the continuous and short fillet welds occurs approximately with the same slope, however, the case with continuous welds experienced greater peak magnitudes of compressive longitudinal stresses than the case with short welds.

5. Conclusions and future work

Simulations of the temperature field, residual stress and angular distortion for the short fillet welds made from S700 were performed by developing three-dimensional FE models in ABAQUS FE code. Two welding sequences and two mechanical boundary conditions were considered in the simulations to study the effect of external restraints and welding sequence on development of angular distortion and residual stresses. The numerical approach was validated through conducting experimental measurements of temperature field, angular distortion and transverse residual stress. A series of comparisons were also made between the cases of continuous and short fillet welds with respect to the temperature field, residual stress and angular distortion. Based on the experimental measurements and numerical results, the following conclusions are made:

(1) The experimental measurement data are in a relatively good agreement with the results of the simulations for temperature fields, angular distortion and transverse residual stresses. It can be concluded that the developed computational approach is able to capture the distributions of the welding residual stresses and angular distortion with acceptable accuracy.
(2) Both the measurement and simulation show that the welding sequence S2 resulted in slightly smaller angular distortion compared to S1 for both of the clamping configurations.
(3) In this study, the external constraints had more influence on the angular distortion than the welding sequence. Using rigid clamping at both ends can significantly prevent angular distortion in continuous fillet welds. For the short fillet welds, using rigid clamping at both ends had a smaller effect on controlling of angular distortion compared to the continuous fillet welds. This matter shows that in practice, controlling of angular distortion due to short fillet welds, apart from using a rigid clamping requires other techniques, such as applying pre-deformations.
(4) The peak stress can easily exceed the yield strength of the material for some of the short fillet welds, especially when clamps with high restraining stiffness are used. In practical applications, this issue should be considered for intermittently fillet welded joints and avoid producing short welds where dynamic loads are introduced, as the high tensile residual stresses can contribute to premature failures, such as fatigue failure.
(5) In short fillet welds, longitudinal residual stress is less sensitive to removal of the rigid clamps than transverse stress. Transverse stress in short fillet welds compared to continuous welds, is less sensitive to the removal of the rigid clamps with high restraining stiffness.
(6) In the stress fields due to each short fillet weld, the differences between peak longitudinal stress magnitudes are smaller than those related to transverse stress. Passing through the HAZ, the gradient of decrease in the longitudinal stress for the short and continuous welds are very similar. Transverse stresses in the short fillet welds, however, have considerably sharper gradients of fall than the continuous fillet welds as moving from the weld toe towards the outer edges.

It was observed in the results that, as the length of the weld decreases, the cooling rate increases. This matter, depending on the steel type, can have a significant impact on the microstructure of the near-weld regions. It is of interest to investigate the effects of the weld length and leg size and consequently cooling rate on the microstructure and deformation patterns of different ultra-high strength steel grades being manufactured with different processes. The aim of this work was to investigate HSSs, and thus the findings of the study are principally limited to these steel grades. However, a future study might also investigate the effect of material strength level on development of residual stresses and distortions in short fillet welds.

CRediT authorship contribution statement

Mehran Ghafouri: Conceptualization, Methodology, Software, Validation, Writing – original draft, Visualization. **Antti Ahola:** Methodology, Writing – review & editing. **Joseph Ahn:** Methodology, Software, Writing – review & editing. **Timo Björk:** Conceptualization, Writing – review & editing, Supervision, Funding acquisition.

Declaration of Competing Interest

The authors declare that they have no known competing financial interests or personal relationships that could have appeared to influence the work reported in this paper.

Acknowledgements

This research was funded by "Finnish Foundation for Technology Promotion" and "Business Finland" (formerly TEKES) in the DigRob research project. The support of SSAB Europe is acknowledged.

Appendix A

A.1. Residual stress components

Distribution of residual stress, in general, comprises both tensile and compressive stresses whose magnitude might reach the yield strength of the material. Distribution, peak magnitude and location of residual stresses, to a great extent, depend on the welding process, external restraints, material properties and geometry of the joint. In the fields of fatigue and fracture mechanics evaluation of welded joints, which are vital topics in structural integrity assessment, the knowledge of residual stress distribution is required. For structural integrity assessment, residual stresses can be generalized based on some invariant features. One technique also known as stress decomposition technique, is used to decompose residual stresses through the thickness. Once distribution of transverse residual stresses over the thickness is available, based on either experimental measurements or FE simulation, residual stress is decomposed into membrane, bending and self-equilibrating stress components, which are described by Eq. (A.1), Eq. (A.2), and Eq. (A.3), respectively:

$$\sigma_{res,m} = \frac{1}{t}\int_0^t \sigma_{res,x}(z)dz \tag{A.1}$$

$$\sigma_{res,b} = \frac{6}{t^2}\int_0^t [\sigma_{res,x}(z) - \sigma_{res,m}]\left(\frac{t}{2} - z\right)\mathrm{d}z \tag{A.2}$$

$$\sigma_{res,se} = \sigma_{res,x} - \sigma_{res,m} - \sigma_{res,b}\left(1 - \frac{2z}{t}\right) \tag{A.3}$$

where $\sigma_{res,m}$, $\sigma_{res,b}$, and $\sigma_{res,se}$ are membrane, bending and self-equilibrating components, respectively. t is material thickness and $\sigma_{res,x}(z)$ is the transverse residual stress in the Z-direction (through thickness). This decomposition technique was applied to CS1 on both sides at the weld toe, and performing integration over the weld length, where $z = 0$ is on the top surface and $z = t$ is on the bottom surface of the specimen. The results regarding the membrane and bending stress components for the clamped and unclamped conditions are shown in Fig. A.1. In addition, Fig. A.1 includes the results of residual stress components for a similar joint being welded continuously over the length of the joint on both sides, where both weld passes were in the same directions.

As can be seen in Fig. A.1, In the case of short welds, and in the clamped conditions, both membrane and bending stress components are high tensile stresses in the location of welds which tend to become compressive in the regions where no welding was performed. The peak tensile stresses of membrane and bending components in short welds are comparably higher than those in continuous welds, which implies that in the case short fillet welds residual stress field is highly localized and dimensionally smaller than those in continuous fillet welds, while the peak magnitudes are comparably larger than those of continuous welds. For example, on side 1 and in the clamped condition, based on Eq. (A.1) and Eq. (A.2), the

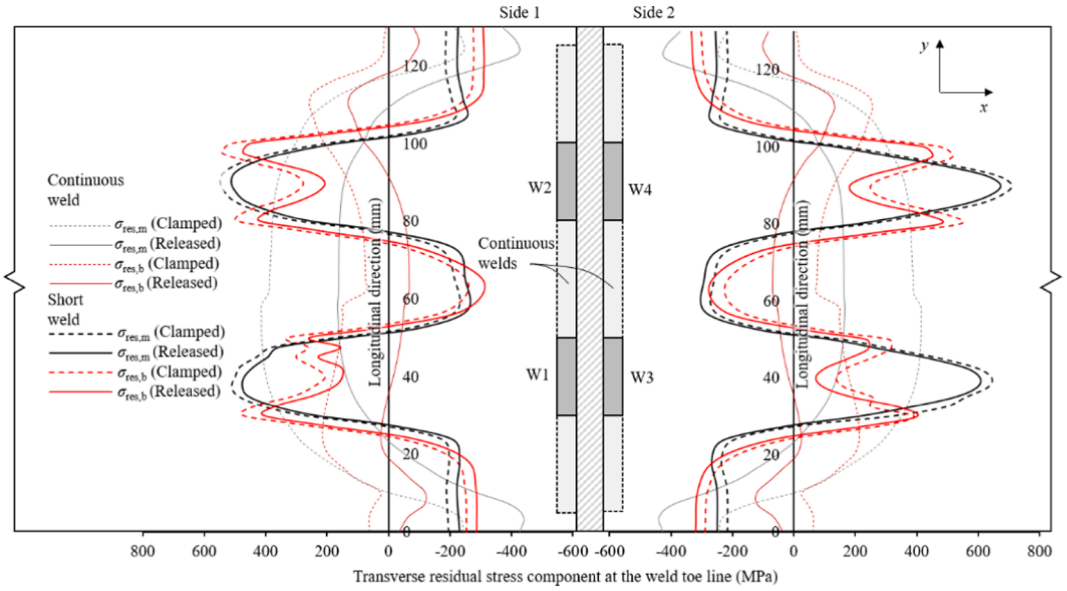

Fig. A1. Membrane and bending components calculated for CS1 at the weld toe in the clamped and released conditions.

membrane and bending stress components of short welds have the peak magnitudes of +547 MPa and +541 MPa, respectively, while these magnitudes for continuous case are +495 MPa and +195 MPa. Provided that the average value over the length of the joint is considered, the membrane and bending stress components for short and continuous welds become +162 MPa, +158 MPa, +238 MPa and +136 MPa, respectively. After removal of the clamps, as can be seen in Fig. A.1, release of both membrane and bending residual stresses in short fillet welds has been done in a smaller extent compared to the continuous fillet welds. The averaged values of membrane and bending components over the length of the joint after release from the clamping in short and continuous welds are +125 MPa, +99 MPa, −7 MPa and −17 MPa, respectively. As can be seen, removal of the clamps had a smaller effect on the residual stress field in short fillet welds than in continuous fillet welds.

The stress decomposition technique presented in this section, which uses the results of the FE welding simulation, is applicable in assessment of the stability of plate components and study of the behavior of crack growth under the influence of an unequal residual stress field, and it can help to estimate the stress intensity factor due to residual stresses [47,48].

References

[1] Conejo AN, Birat J-P, Dutta A. A review of the current environmental challenges of the steel industry and its value chain. J Environ Manage 2020;259:109782.

[2] Guo W, Crowther D, Francis JA, Thompson A, Liu Z, Li L. Microstructure and mechanical properties of laser welded S960 high strength steel. Mater Des 2015;85:534–48. https://doi.org/10.1016/J.MATDES.2015.07.037.

[3] Liang W, Deng D. Influences of heat input, welding sequence and external restraint on twisting distortion in an asymmetrical curved stiffened panel. Adv Eng Softw 2018;115:439–51. https://doi.org/10.1016/J.ADVENGSOFT.2017.11.002.

[4] Skriko T, Ghafouri M, Björk T. Fatigue strength of TIG-dressed ultra-high-strength steel fillet weld joints at high stress ratio. Int J Fatigue 2017;94:110–20. https://doi.org/10.1016/j.ijfatigue.2016.09.018.

[5] Deng D, Liu X, He J, Liang W. Investigating the influence of external restraint on welding distortion in thin-plate bead-on joint by means of numerical simulation and experiment. Int J Adv Manuf Technol 2016;82(5-8):1049–62.

[6] Barsoum Z, Lundbäck A. Simplified FE welding simulation of fillet welds - 3D effects on the formation residual stresses. Eng Fail Anal 2009;16(7):2281–9. https://doi.org/10.1016/j.engfailanal.2009.03.018.

[7] Barsoum Z, Barsoum I. Residual stress effects on fatigue life of welded structures using LEFM. Eng Fail Anal 2009;16(1):449–67. https://doi.org/10.1016/j.engfailanal.2008.06.017.

[8] Cui C, Zhang Q, Bao Y, Bu Y, Luo Y. Fatigue life evaluation of welded joints in steel bridge considering residual stress. J Constr Steel Res 2019;153:509–18. https://doi.org/10.1016/J.JCSR.2018.11.003.

[9] Jiang W, Xie X, Wang T, Zhang X, Tu S-T, Wang J, et al. Fatigue life prediction of 316L stainless steel weld joint including the role of residual stress and its evolution: Experimental and modelling. Int J Fatigue 2021;143:105997.

[10] Heinze C, Schwenk C, Rethmeier M. Numerical calculation of residual stress development of multi-pass gas metal arc welding. J Constr Steel Res 2012;72:12–9. https://doi.org/10.1016/j.jcsr.2011.08.011.

[11] Deng D. FEM prediction of welding residual stress and distortion in carbon steel considering phase transformation effects. Mater Des 2009;30(2):359–66. https://doi.org/10.1016/j.matdes.2008.04.052.

[12] Liang W, Hu X, Zheng Y, Deng D. Determining inherent deformations of HSLA steel T-joint under structural constraint by means of thermal elastic plastic FEM. Thin-Walled Struct 2020;147:106568. https://doi.org/10.1016/j.tws.2019.106568.

[13] Ma N, Cai Z, Huang H, Deng D, Murakawa H, Pan J. Investigation of welding residual stress in flash-butt joint of U71Mn rail steel by numerical simulation and experiment. Mater Des 2015;88:1296–309. https://doi.org/10.1016/J.MATDES.2015.08.124.

[14] Wu J, Qiang B, Liao X, Kang L, Yao C, Li Y. Experimental investigation and numerical simulation of welding residual stress in orthotropic steel deck with diaphragm considering solid-state phase transformation. Eng Struct 2022;250:113415.

[15] Rikken M, Pijpers R, Slot H, Maljaars J. A combined experimental and numerical examination of welding residual stresses. J Mater Process Technol 2018;261:98–106. https://doi.org/10.1016/j.jmatprotec.2018.06.004.

[16] Ghafouri M, Ahn J, Mourujärvi J, Björk T, Larkiola J. Finite element simulation of welding distortions in ultra-high strength steel S960 MC including comprehensive thermal and solid-state phase transformation models. Eng Struct 2020;219:110804. https://doi.org/10.1016/j.engstruct.2020.110804.

[17] Ahn J, He E, Chen L, Pirling T, Dear JP, Davies CM. Determination of residual stresses in fibre laser welded AA2024-T3 T-joints by numerical simulation and neutron diffraction. Mater Sci Eng, A 2018;712:685–703. https://doi.org/10.1016/j.msea.2017.12.027.

[18] Hemmesi K, Farajian M, Boin M. Numerical studies of welding residual stresses in tubular joints and experimental validations by means of x-ray and neutron diffraction analysis. Mater Des 2017;126:339–50. https://doi.org/10.1016/J.MATDES.2017.03.088.

[19] Jiang W, Chen W, Woo W, Tu ST, Zhang XC, Em V. Effects of low-temperature transformation and transformation-induced plasticity on weld residual stresses: Numerical study and neutron diffraction measurement. Mater Des 2018;147:65–79. https://doi.org/10.1016/J.MATDES.2018.03.032.

[20] Wan Yu, Jiang W, Song M, Huang Y, Li J, Sun G, et al. Distribution and formation mechanism of residual stress in duplex stainless steel weld joint by neutron diffraction and electron backscatter diffraction. Mater Des 2019;181:108086.

[21] Sun J, Liu X, Tong Y, Deng D. A comparative study on welding temperature fields, residual stress distributions and deformations induced by laser beam welding and CO2 gas arc welding. Mater Des 2014;63:519–30. https://doi.org/10.1016/j.matdes.2014.06.057.

[22] Lee C-H, Chang K-H. Prediction of residual stresses in high strength carbon steel pipe weld considering solid-state phase transformation effects. Comput Struct 2011;89(1-2):256–65. https://doi.org/10.1016/j.compstruc.2010.10.005.

[23] Jin D, Hou C, Shen L. Effect of welding residual stress on the performance of CFST tubular joints. J Constr Steel Res 2021;184:106827.

[24] Evdokimov A, Doynov N, Ossenbrink R, Obrosov A, Weiß S, Michailov V. Thermomechanical laser welding simulation of dissimilar steel-aluminum overlap joints. Int J Mech Sci 2021;190:106019.

[25] Ahn J, He E, Chen L, Wimpory RC, Dear JP, Davies CM. Prediction and measurement of residual stresses and distortions in fibre laser welded Ti-6Al-4V considering phase transformation. Mater Des 2017;115:441–57. https://doi.org/10.1016/J.MATDES.2016.11.078.

[26] Danis Y, Lacoste E, Arvieu C. Numerical modeling of inconel 738LC deposition welding: Prediction of residual stress induced cracking. J Mater Process Technol 2010;210(14):2053–61. https://doi.org/10.1016/j.jmatprotec.2010.07.027.

[27] Yaghi AH, Hyde TH, Becker AA, Sun W, Wen Wu, Hilson G, et al. Comparison of measured and modelled residual stresses in a welded P91 steel pipe undergoing post weld heat treatment. Int J Press Vessel Pip 2020;181:104076.

[28] Hu X, Feng G, Wang Y, Zhang C, Deng D. Influence of lumping passes on calculation accuracy and efficiency of welding residual stress of thick-plate butt joint in boiling water reactor. Eng Struct 2020;222:111136. https://doi.org/10.1016/j.engstruct.2020.111136.

[29] Deng D, Liang W, Murakawa H. Determination of welding deformation in fillet-welded joint by means of numerical simulation and comparison with experimental measurements. J Mater Process Technol 2007;183(2-3):219–25.

[30] Khedmati MR, Rastani M, Ghavami K. Numerical study on the permissible gap of intermittent fillet welds of longitudinally stiffened plates under in plane axial compression. J Constr Steel Res 2007;63(10):1415–28.

[31] Perić M, Tonković Z, Rodić A, Surjak M, Garašić I, Boras I, et al. Numerical analysis and experimental investigation of welding residual stresses and distortions in a T-joint fillet weld. Mater Des 2014;53:1052–63.

[32] Zhang Y, Wang Y. The influence of welding mechanical boundary condition on the residual stress and distortion of a stiffened-panel. Mar struct 2019;65:259–70. https://doi.org/10.1016/J.MARSTRUC.2019.02.007.

[33] Fu G, Lourenco MI, Duan M, Estefen SF. Effect of boundary conditions on residual stress and distortion in T-joint welds. J Constr Steel Res 2014;102:121–35. https://doi.org/10.1016/J.JCSR.2014.07.008.

[34] Ghafouri M, Ahola A, Ahn J, Björk T. Welding-induced stresses and distortion in high-strength steel T-joints: Numerical and experimental study. J Constr Steel Res 2022;189:107088.

[35] ABAQUS user's manual, Version; 2020.

[36] Goldak J, Chakravarti A, Bibby M. A new finite element model for welding heat sources. Metall Trans B 1984;15(2):299–305. https://doi.org/10.1007/BF02667333.

[37] Siltanen J, Tihinen S, Kömi J. Laser and laser gas-metal-arc hybrid welding of 960 MPa direct-quenched structural steel in a butt joint configuration. J Laser Appl 2015;27:S29007. https://doi.org/10.2351/1.4906386.

[38] Deng D, Murakawa H, Liang W. Numerical simulation of welding distortion in large structures. Comput Methods Appl Mech Eng 2007;196(45-48):4613–27.

[39] Shen J, Chen Z. Welding simulation of fillet-welded joint using shell elements with section integration. J Mater Process Technol 2014;214(11):2529–36.

[40] Seleš K, Perić M, Tonković Z. Numerical simulation of a welding process using a prescribed temperature approach. J Constr Steel Res 2018;145:49–57. https://doi.org/10.1016/J.JCSR.2018.02.012.

[41] Bhatti AA, Barsoum Z, Murakawa H, Barsoum I. Influence of thermo-mechanical material properties of different steel grades on welding residual stresses and angular distortion. Mater Des 2015;65:878–89. https://doi.org/10.1016/j.matdes.2014.10.019.

[42] Brickstad B, Josefson BL. A parametric study of residual stresses in multi-pass butt-welded stainless steel pipes. Int J Press Vessel Pip 1998;75(1):11–25. https://doi.org/10.1016/S0308-0161(97)00117-8.

[43] Yaghi A, Hyde TH, Becker AA, Sun W, Williams JA. Residual stress simulation in thin and thick-walled stainless steel pipe welds including pipe diameter effects. Int J Press Vessel Pip 2006;83(11-12):864–74. https://doi.org/10.1016/j.ijpvp.2006.08.014.

[44] Ferro P, Berto F, Bonollo F, Tang K. Does metallurgy affect the residual notch stress intensity factor value induced by welding operations? A comprehensive study via a 3D numerical model. Int J Fatigue 2021;149:106261.

[45] Björk T, Ahola A, Tuominen N. On the design of fillet welds made of ultra-high-strength steel. Weld World 2018;62(5):985–95.
[46] Amraei M, Ahola A, Afkhami S, Björk T, Heidarpour A, Zhao X-L. Effects of heat input on the mechanical properties of butt-welded high and ultra-high strength steels. Eng Struct 2019;198:109460. https://doi.org/10.1016/j.engstruct.2019.109460.
[47] Bhardwaj S, Chandima Ratnayake RM. Residual stress estimation in defect assessment procedures at weld toe and away locations on girth welds: Review of key parameters. Theor Appl Fract Mech 2021;111:102848.
[48] Dong P. Length scale of secondary stresses in fracture and fatigue. Int J Press Vessel Pip 2008;85(3):128–43.